DEVELOPMENT OF POLARIZING SPECTRAL BANDPASS FILTER USING DUAL SUBWAVELENGTH METALLIC GRATINGS

by

Andrew Joseph Hohne

A thesis submitted in partial fulfillment
of the requirements for the degree

of

Master of Science

in

Electrical Engineering

MONTANA STATE UNIVERSITY
Bozeman, Montana

July, 2017

©COPYRIGHT

by

Andrew Joseph Hohne

2017

All Rights Reserved

DEDICATION

I dedicate this to my parents, Bob and Patti, who supported and encouraged me in every way during my long academic career.

ACKNOWLEDGMENTS

I would like to take this opportunity to thank my advisor Dr. Wataru Nakagawa in the Department of Electrical and Computer Engineering at Montana State University for his guidance and encouragement over the past two and half years. In his research group he created an environment of academic openness and a strong work ethic that ultimately led me to the completion of this research. His example is one I hope to follow in my future work.

I would also like to thank my other committee members, Dr. Joseph A. Shaw and Dr. David L. Dickensheets from the Electrical and Computer Engineering Department for agreeing to a be part of my defense and for their invaluable contributions to this NASA project.

I am also indebted to my office mates Martin and Tianbo for always being willing to read my writing and for teaching me how to use LaTeX.

Most importantly, I would like to thank my siblings Rob, Mike, and Kate, and especially my parents Bob and Patti for their unconditional support during all the years that led to this moment. I couldn't have done this without them.

Funding Acknowledgment

This work was kindly supported by NASA EPSCoR grant NNX14AN40A: Nanostructured Polarization Optics for Atmospheric Remote Sensing

TABLE OF CONTENTS

1. INTRODUCTION 1

General 1
Polarization "Bayer" Filter 2
Simultaneous Wavelength Selectivity 3
Conclusion 8

2. THEORY OF OPERATION 10

Overview 10
Background 10
Zero-order Effective Medium Theory (EMT) 11
The Wire Grid Polarizer 13
Diffraction Gratings 13
Surface Plasmon Polaritons (SPP) 14
Rigorous Coupled-Wave Analysis (RCWA) 15
Fabry-Perot Resonance (FP) 16
FP resonance between gratings 16
FP Resonance in Bottom Layer 21
TM Transmission Minima at SPP Excitation Frequencies 22
SPP/FP Coupling 23
Conclusion 24

3. CHARACTERIZATION AND MODEL IMPROVEMENT 27

Overview 27
Background 27
Preliminary Design 27
Fabrication 27
White Light Spectral Test System 28
Comparison of Simulation to Test Results 29
Improvement to Model 29
Material Properties 30
Gold Dielectric Function 30
Silicon Dielectric Function 31
Geometry 31
Discrepancy Between Experiment and Simulation from Parameter Tolerances 37
Grating Separation 37
Fill Factor 38

TABLE OF CONTENTS — CONTINUED

Gold Depth 38
Conclusion 38

4. SILICON DEVICE DESIGN 41

Overview 41
Introduction 41
Period and Silicon Fill Factor 41
Grating Separation, Gold Fill Factor, and Gold Depth 43
Global Optimization 48
Tolerance Analysis 54
Conclusion 54

5. GENERAL DIELECTRIC DESIGN 58

Overview 58
Design Considerations 58
Square Side Walls 58
High Fill Factor 59
Variable Dielectric Constant for Grating 59
SPP Resonance Separation 59
Fill Factor Selection 59
Design Procedure 61
Parameter Optimization 66
Conclusion 70

6. CONCLUSION 73

Summary 73
Discussion 74
Future Work 75

REFERENCES CITED 77

LIST OF TABLES

Table		Page
4.1	Global device optimization parameters	48
4.2	Optimized family of filters designs with peak TM transmission between 1527 nm and 1679 nm	49
5.1	1700-nm parameter optimization	67
5.2	1640-nm parameter optimization	67
5.3	1550-nm parameter optimization	68
5.4	Selection criteria	68
5.5	Optimization results	68
5.6	Final optimization results	70

LIST OF FIGURES

Figure		Page
1.1	The arrangement of a hypothetical single-wavelength imaging polarimeter	3
1.2	Wavefront division polarimetry of clouds	4
1.3	The arrangement of a hypothetical three-wavelength imaging polarimeter	5
1.4	Broadband polarizer to spectral bandpass filter	6
1.5	A single grating layer buried in magnesium fluoride and coated with PMMA	6
1.6	Sun group spectral filter/polarizers	7
2.1	Cross section of proposed device	11
2.2	Effective medium theory	12
2.3	Rigorous coupled-wave analysis	16
2.4	Real part of TM effective index of refraction for each layer of device as a function of fill factor	18
2.5	Imaginary part of TM effective index of refraction for each layer of device as a function of fill factor	18
2.6	Real part of TE effective index of refraction for each layer of device as a function of fill factor	19
2.7	Imaginary part of TE effective index of refraction for each layer of device as a function of fill factor	19
2.8	Plot of the positions of the FP peak wavelengths with changing grating gap and mode number.	20
2.9	RCWA simulations showing TM transmittance as a function of grating separation and wavelength	20
2.10	RCWA simulations showing TE transmittance as a function of grating separation and wavelength	21
2.11	Two different metal-dielectric interfaces allow for the presence of two different SPP resonances	22

LIST OF FIGURES — CONTINUED

Figure		Page
2.12	Log plot of TM transmission as a function of grating gap and wavelength.	23
2.13	Electric field strength of a normal FP resonance	24
2.14	Near SPP resonance, the field becomes more localized in dielectric pillars raising the effective index of the middle region.	25
2.15	FP resonance turns off and new resonance appears where anti-FP resonance would be in the absence of an SPP	25
3.1	An SEM image of a completed 80-micron by 80-micron grating	28
3.2	Characterization set-up	29
3.3	Experimental results of polarization spectral filter	30
3.4	Large range of measured dispersion curves for gold in the shortwave infrared region.	31
3.5	Silicon material properties	32
3.6	Varying gold material properties	32
3.7	Varying silicon material properties	33
3.8	Image of a cross section of a grating	34
3.9	Examples of device geometries used to investigate the effect of narrow silicon pillars on device performance.	34
3.10	Increasing the narrowness of the silicon pillars blue shifted the spectrum.	35
3.11	Simulation geometry using separate fill factors for gold and dielectric	35
3.12	Simulation vs experiment after model improvements for TM	36
3.13	Simulation vs experiment after model improvements for TE	36
3.14	Effect of gap tolerances	37
3.15	Effect of fill factor tolerances	38
3.16	Effect of gold thickness tolerances	39

LIST OF FIGURES — CONTINUED

Figure Page

3.17 Experimental vs simulation results of broader spectrum polarizer using improvements to model 40

4.1 Choosing silicon fill factor and period for silicon on quartz device 42

4.2 Log plot of the transmission spectra as a function of grating gap 44

4.3 Linear plot of the transmission spectra as a function of gap 45

4.4 Effect of gold depth on silicon on quartz performance 46

4.5 If the etch depth is too small or too large, wings appear either to the right or left of the main peak. 47

4.6 Choosing a middle etch depth far away from other FP resonances results in the best spectrum. 47

4.7 Scoring in the global optimization of silicon on quartz design 50

4.8 Scatter plot of scoring results for global optimization of silicon on quartz device — 1 50

4.9 Scatter plot of scoring results for global optimization of silicon on quartz device — 2 51

4.10 Scatter plot of scoring results for global optimization of silicon on quartz device — 3 51

4.11 Family of optimized silicon on quartz devices in parameter space 52

4.12 Transmission TM spectra of optimized silicon on quartz devices 53

4.13 Optimum design of device at operating wavelength of 1550 nm 53

4.14 Silicon on quartz gap tolerance effect 55

4.15 Silicon on quartz gold tolerance effect 55

4.16 Silicon on quartz period tolerance effect 56

4.17 Silicon on quartz gold fill factor tolerance effect 56

LIST OF FIGURES — CONTINUED

Figure		Page
4.18	Silicon on quartz silicon fill factor tolerance effect	57
5.1	Required grating dielectric constant as a function of desired anchor point separation	60
5.2	Choosing grating dielectric constant and period for variable index grating design	62
5.3	Offset between simulation and EMT	63
5.4	Effect of grating gap on variable index grating design	64
5.5	Effect of gold thickness on variable index grating design	65
5.6	Three channel filter TM spectra pre-optimization based on variable index grating design	66
5.7	Three channel filter TE spectra pre-optimization based on variable index grating design	67
5.8	TM spectra on three channels before and after optimization for variable index grating design	69
5.9	A cross section of the 1550-nm design.	71
5.10	A cross section of the 1640-nm design.	71
5.11	A cross section of the 1700-nm design.	72

ABSTRACT

Recent work in climate science has shown the need for a polarizing spectral bandpass filter in order to passively and remotely determine cloud water phase. Presented here is a novel design of such a filter based on two subwavelength gold gratings separated by a dielectric surface relief grating. It is shown that a Fabry-Perot resonance occurs in the cavity between the gold gratings while surface plasmon polariton resonances occur at the two metal/dielectric interfaces. It is further shown that these two resonance effects couple together to create a spectral bandpass that is high and narrow enough for the remote sensing application. These resonance effects can be changed in shape and position by adjusting the width, height, period, and separation between the gold gratings. It is further observed that the surface plasmon polariton resonances also have the effect of suppressing light transmission at certain wavelengths, allowing the spectral bandpass shape to be tuned, reducing out-of-band transmission. The polarizing effect of these gratings results from the rejection of light polarized along the grating rulings, a phenomenon that is well documented to occur in subwavelength wire grids. Experimental data on prototype gratings show good agreement with predicted performance calculated using numerical rigorous-coupled wave analysis once we account for uncertainties in the material properties and device geometry due to fabrication and processing variabilities. This numerical method is used in conjunction with analytical approximations like zero-order effective medium theory to develop a design process that can be extended to any wavelength in the shortwave infrared region. All devices undergo a final global parameter optimization procedure to account for any subtle near-field effects. Finally, I present designs of three devices optimized for operation at wavelengths of 1550 nm, 1640 nm, and 1700 nm. These devices share characteristics that make them able to be simultaneously fabricated on the same substrate, a crucial step if they are to be built into an array. The final devices all have a peak transmission of greater than 80%, and spectral widths of less than 40 nm.

1

INTRODUCTION

General

Around 75% of the earth is covered by clouds at any given time, according to a two-decade study between 1979 and 2001 [1]. In order to understand their thermal and radiometric properties, and therefore their effect on the earth's climate, we must understand their composition [2], more specifically the phase of the water they contain. While lidar techniques have already been shown to classify ice clouds [3], it requires active illumination which limits the field of view. What is needed is an imaging system that can determine the water phase of clouds in a large, passively illuminated scene. Some work has already been done that suggests polarization information of scattered sunlight off clouds can be used to determine cloud phase [4].

The polarization of an electromagnetic wave is defined as the preferred direction the electric field vector. Light is called "unpolarized" or randomly polarized when there is on average no predominant electric field direction. The polarization state of light can be represented by four values called Stokes parameters, (S_0, S_1, S_2, S_3). The S_0 parameter corresponds to the intensity of light while the S_1 and S_2 parameters correspond to light that is polarized along the horizontal/vertical axes and $45°/-45°$ axes, respectively. The S_3 parameter corresponds to the degree of circular polarization. For example, $(1, 0, 0, 0)$ represents unpolarized light, while $(1, 1, 0, 0)$ represents light that is polarized in the horizontal direction. If S_1 is oppositely signed, $(1, -1, 0, 0)$, then the state represents light polarized in the vertical direction [5]. Right-hand and left-hand circular polarized light are represented by $(1, 0, 0, 1)$ and

$(1, 0, 0, -1)$, respectively. Since the amount of linearly polarized light in scattered sunlight is the quantity of interest, circular polarization will not be considered.

Polarization isn't the only property of light that can be exploited to remotely determine cloud phase. Recent modeling work at Montana State University [6] showed that we can determine cloud phase if we make differential radiometric measurements of scattered cloud light at two or three infrared wavelengths (1550 nm, 1640 nm, 1700 nm).

What is described in the following work is an attempt to design a device that utilizes both the polarization and spectral characteristics of scattered sunlight. To do this we need to introduce the concept of the polarization "Bayer" filter. We will then expand that concept to include wavelength selectivity in order to create a filter that can select for both polarization and wavelength.

Polarization "Bayer" Filter

To recover the first three Stokes parameters, we need to image a scene using three different polarizer orientations. This process of determining the polarization content of a scene is called polarimetry. Traditional polarimetry involves a time-multiplexed signal. Multiple images of a scene are taken in succession, each with a different orientation of a linear polarizer. A different kind of polarimeter involves spatial multiplexing by pairing each detector pixel with a similarly sized micro-grating. This is called wavefront division polarimetry [7,8]. By grouping four adjacent pixels together as a superpixel similar to a color Bayer filter (Figure 1.1), one can determine the polarization content of a scene with one image, at the expense of some resolution (Figure 1.2). There are currently imaging polarimeters on the market, such as the PolarCam, made by 4D Technology, which indeed utilizes a polarization "Bayer" filter [9]. However, these polarimeters have broadband wavelength response

which make them unable to select for wavelength, which is one of the goals of this work.

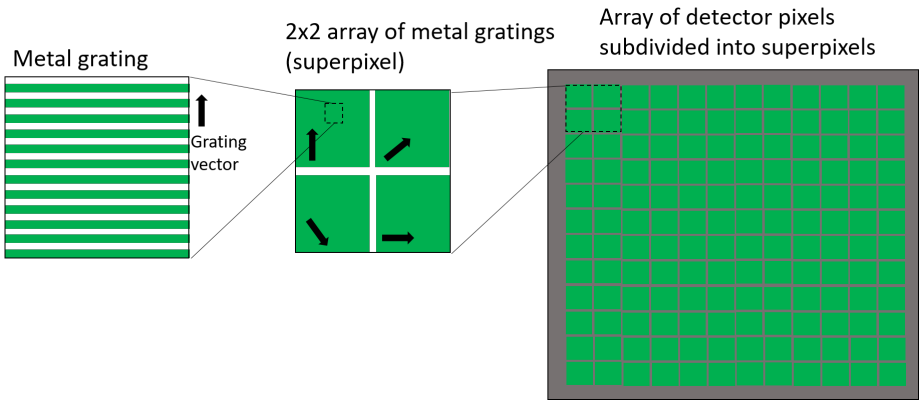


Figure 1.1: The arrangement of a hypothetical single-wavelength imaging polarimeter: The detector pixels are subdivided into groups of four and overlaid with 2x2 arrays of metals gratings of four orientations. In principle we only need three grating directions, but here we have a redundant direction to accommodate the square layout of the detector array.

Simultaneous Wavelength Selectivity

Recent work at Montana State University has shown that that broadband polarimetric measurements of clouds can be improved upon if we are also able to resolve wavelength [6]. Therefore, instead of making four measurements per superpixel, we need to make nine measurements per superpixel (three orientations for each wavelength: 1550 nm, 1640 nm, 1700 nm). Since the polarization "Bayer" filter has already been demonstrated, we can extend this concept to allow for simultaneous wavelength selectivity. For a single wavelength (or range of wavelengths) the detector pixels need to be subdivided into groups of four (three primary orientations, three redundant). If we add two more wavelength channels for a total of three, the detectors

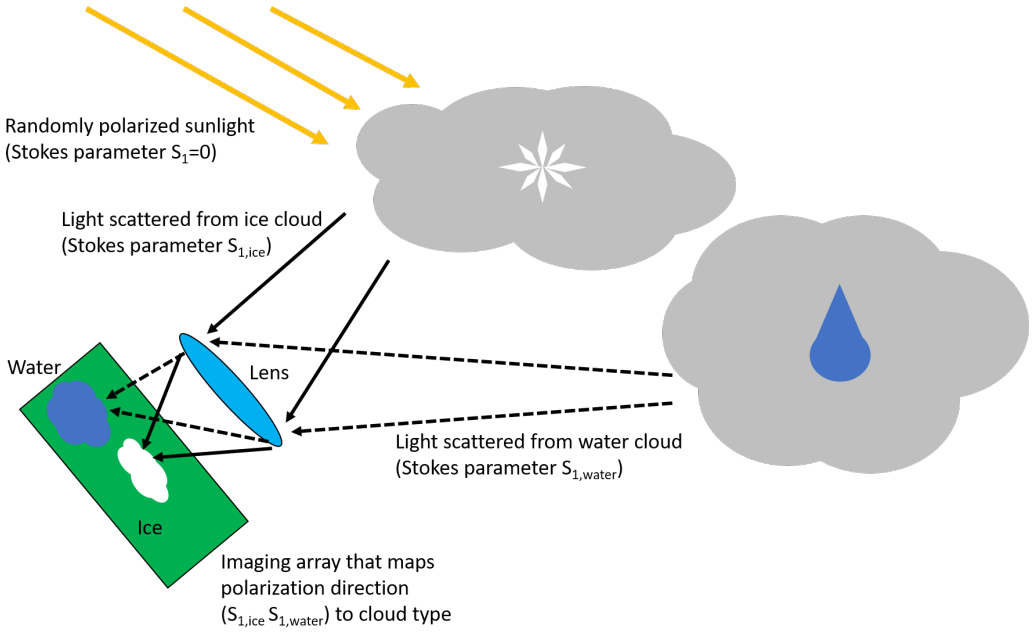


Figure 1.2: Unpolarized sunlight scattering off clouds will have a different direction of linear polarization depending on whether the cloud is composed of liquid water droplets or ice particles (This is represented by the Stokes parameter S_1). By imaging the scattered light onto an array of polarization Bayer filters, we can determine cloud phase.

must now be subdivided into groups of nine (three orientations, three channels) (Figure 1.3).

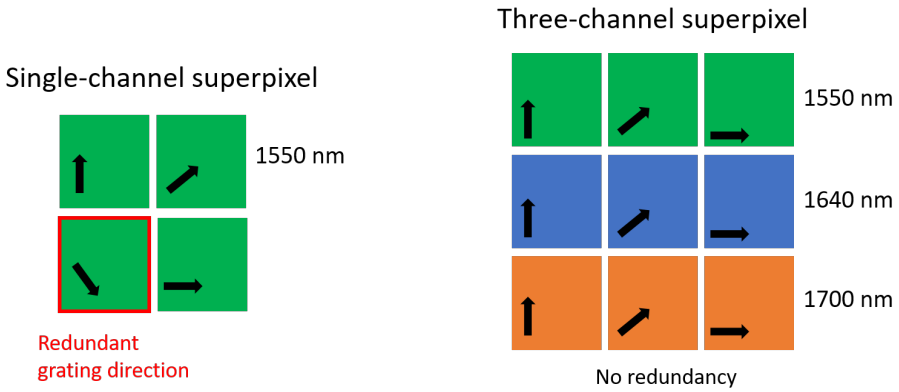


Figure 1.3: The arrangement of a hypothetical three-wavelength imaging polarimeter: The detector pixels are subdivided into groups of nine and overlaid with 3x3 arrays of metals gratings of three orientations. In contrast to the single-channel case, a redundant grating orientation is not needed to accommodate the square layout of the detector array.

While it would be possible, in principle, to simply build polarizers and spectral filters separately and mate them together, it would be advantageous both for system integration and light throughput to have a grating geometry that is able to select both for polarization and for wavelength.

Spectral filtering behavior has already been documented in single-layer gratings. For example, researchers at the University of Michigan have shown that by increasing the period of a metal-on-dielectric nano-slit grating, the transmission spectrum changes from that of a polarizer (wide bandpass) to a spectral filter (narrow bandpass) [10]. Simulation results have shown that such single-grating structures can be used as color filters, specifically for use in liquid crystal display technology [11]. The results of both studies show spectral filters that are asymmetric, with the longer-wavelength side (right side) of the spectral filters being more transmissive than the left side.

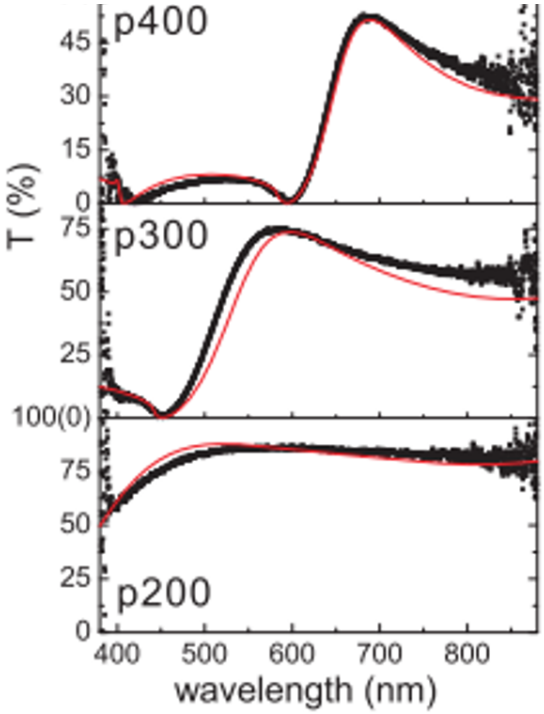


Figure 1.4: As the period of the single-layer aluminum grating is increased from 200 nm to 400 nm, the transmission spectrum of the TM polarization changes from broadband to a spectral bandpass. Figure courtesy of [10].

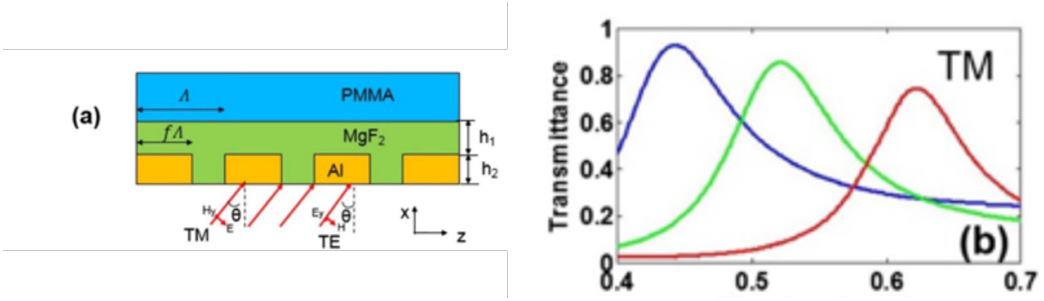


Figure 1.5: A single grating layer buried in magnesium fluoride and coated with PMMA behaves like a color filter in the visible spectrum for applications in liquid crystal display technology. (a) Grating geometry. (b) Different values of f and Λ result in different color filters. Figure courtesy of [11].

Others studies show with simulation that a more complex geometry - a single-layer metal grating with grooves carved in each ruling - could improve the bandpass shape [12]. Surface plasmon resonances and resonances within the carved groove suppressed transmission on either side of the transmission resonance. Nguyen-Huu et al. [13] used a genetric algorithm to determine the parameters of a two-layer metallic grating that had improved spectral performance of Luo's device. However, it suffered from high absorption and a geometry that would be difficult to fabricate since some of the features were as small as 5 nm.

Sun et al. succeeded in designing and fabricating a polarization-selective bandpass filter in the visible spectrum [14]. This geometry (Figure 1.6), similar to our own final device, was designed to be a novel display technology.

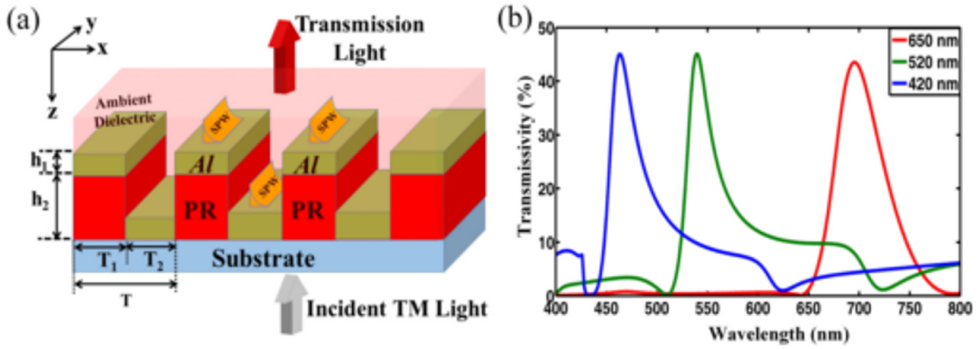


Figure 1.6: The left side (a) shows their two-layer aluminum grating separated by a layer of photoresist fabricated on top of a glass substrate. The simulation results on the right side (b) show excellent wavelength selectivity in the visible domain. Figure courtesy of [14]

A different attempt at a color-selective polarization Bayer filter has been done by Junger et al. by placing a nanostructured array of holes on top of a CMOS photodiode to achieve wavelength selectivity, then overlaying the detectors with the same four-orientation pattern discussed above [15].

8

Conclusion

The single-grating designs described by Zhou and Luo both produced spectra that had very low TM transmission on the left side of the bandpass, but a non-zero transmission on the right side. Since these filters were intended for LCD applications, the out-of-band transmission would not be much of a problem for that application. However, for our climate science application, we would like the out-of-band transmission to be as low as possible.

The more complicated geometries, like the single-layer grating with grooves, or the two-layer offset gratings, both present fabrication issues. Patterning the top of a metal grating could be done with a focused ion beam mill, a tool which is not present at our facilities. Nguyen-Huu's design required line widths of around 5 nm which might be difficult to reliably reproduce. While Sun et al. ended up utilizing some of the same physical principles as our final design, the material they used for fabricating the dielectric grating is electron-beam resist. High aspect ratio structures are possible using resists such as PMMA, but they require very high voltage electron beam lithography [16]. They are also less rigid than other materials like silicon and silicon nitride. The individual parts of the CMOS design are not difficult to make, in principle, but would have to be manufactured separately and then mated together, which defeats the purpose of the single device goal.

My goal was to develop a design procedure to produce the appropriate polarization-selective spectral bandpass filters at the three design wavelengths. These will be used to determine the Stokes parameters of sunlight scattered from clouds at each wavelength. In order to understand the effect that each grating parameter will have on performance, I had to analyze the complex physical phenomena occurring within the grating.

With the assistance of others I also fabricated and optically characterized some of these gratings to ascertain how well the simulation model reflects reality. Results of the spectral measurements that would reflect differences in material properties and non-ideal device geometry were fed back into the simulation models.

10

THEORY OF OPERATION

Overview

As discussed in the introduction, the design goal was a two-layer subwavelength grating that rejects as much incident TE light as possible. Only TM light of a certain wavelength was to be allowed to transmit. To do this, we utilized a device architecture that was originally intended to be a broadband polarizing beam splitter, where TE was reflected over a broadband spectrum and TM was transmitted over a broadband spectrum. In order to limit TE at all wavelengths and further restrict TM transmission, we required a good understanding of the effect of changing various parameters. There are a variety of physical phenomena that can occur when light interacts with structures that are smaller than its wavelength and the complicated coupling between all these phenomena make exact analytical solutions difficult or impossible. In this section I describe various nanoscale optical phenomena as well as analytic approximations and simulation techniques used in subsequent sections to design the device.

Background

The basic design, seen in Figure 2.1, consists of a surface relief grating that is coated with gold. The end result is essentially two metallic wire grids separated by a resonant cavity. In earlier devices, the grating material in the substrate material were the same, but in general they are different. Earlier devices with similar geometries included a reflective quarter-wave plate to be used for ultra-compact microscopy, and a polarizing beam splitter.

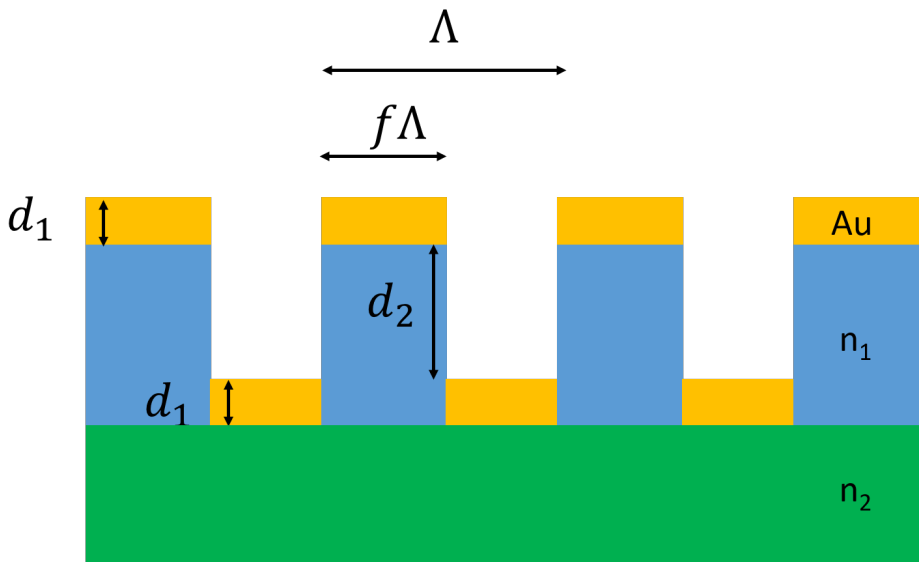


Figure 2.1: Cross section of the device. Gold is deposited onto a dielectric grating of index n_1 which lies on top of a substrate of index n_2. Λ is the grating period, f is the fill factor, d_2 is the separation between the two metallic gratings, and d_1 is gold depth.

Zero-order Effective Medium Theory (EMT)

Consider periodically stratified media (Figure 2.2 where light is propagating normal to the direction of stratification. If the wavelength of light is much larger than the period of stratification, we can make the reasonable approximation that either the electric field $\vec{E}$ or the electric field displacement $\vec{D}$ are constant across a period of the media. Which field is constant depends on the polarization of the incident light. This means we can treat the stratified medium as two different effective bulk media for both TE- and TM-polarized light. From Maxwell's boundary conditions we know that the tangential component of the $\vec{E}$ is constant at the interface between two dielectrics. For the TE case, if we consider an average $\vec{D}$ we can arrive at Equation 2.1 for the effective dielectric constant. By contrast, the normal component of $\vec{D}$ is continuous at material boundaries. Therefore, for TM polarization, by considering an average $\vec{E}$, the same constitutive relation gives us a different expression for the

bulk dielectric of the same structure. This type of birefringence that occurs with subwavelength-scale structuring of isotropic material is called form birefringence [17].

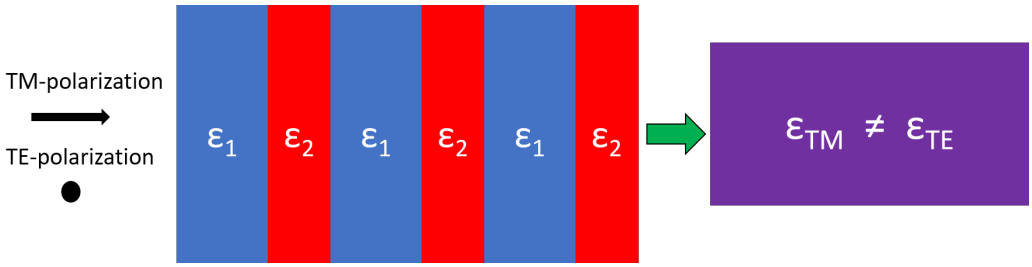


Figure 2.2: Periodically stratified media can be represented as a homogeneous material when light propagates normal to the direction of stratification and when the wavelength of light is much larger than the period of stratification.

The formulae for the TE and TM dielectric permittivities when the wavelength of light is much greater than the period of stratification are

$$\epsilon_{TE} = f\epsilon_1 + (1-f)\epsilon_2 \tag{2.1}$$

and

$$\frac{1}{\epsilon_{TM}} = \frac{f}{\epsilon_1} + \frac{1-f}{\epsilon_2}, \tag{2.2}$$

where ϵ_1 and ϵ_2 are the dielectric constants of the two materials in the periodic layer and f is the fill factor, the fraction of the period that is composed of material 1 [18]. For example, looking at Figure 2.1 the first layer would have $\epsilon_1 = \epsilon_{Au}$ and $\epsilon_2 = 1$.

This is known as zero-order effective medium theory (EMT) when the effective permittivities have no dependence on period. In reality, our grating structures are closer to the wavelength of light, so Equations 2.1 and 2.2 don't strictly apply. However, they will still be used to qualitatively describe device behavior. Higher-order effective medium theories exist, but are much more complicated without giving much more physical insight [19].

The Wire Grid Polarizer

The polarizing effect of wire grid polarizers is well understood from a theoretical standpoint [5] and has been well documented in the near-infrared region [20]. The rejection of the TE mode (polarized normal to the grating vector) is high over a large wavelength range. The high reflectivity for TE polarization is explained best by considering the effective index according to Equation 2.1. The real part of the dielectric of gold is -100, while it is unity for air which means that $\epsilon_{TE} < 0$. This means that the TE radiation sees the first layer of the device as a metal, and is therefore largely reflected. On the other hand, the real part of ϵ_{TM} turns out to be positive, which means the TM radiation sees an effective dielectric layer which has a much lower reflectivity. This difference in reflectivity depending on polarization is what makes the metallic wire-grid an effective polarizer.

Diffraction Gratings

The period of our gratings have to be small enough such that we don't get any first-order diffraction. When light is incident on a grating, integer multiples of the grating wave vector are added to the wave vector of the incident light, leading to wavefronts that diffract away from the grating at angles that increase with integer number. Transmitted light with zero multiples of the grating vector is not diffracted at all, while transmitted light with one, two, three multiples of the grating vector are referred to as first, second, third diffraction orders. Higher diffraction orders deflect light at an angle determined by the surrounding refractive indices and the integer order of diffraction. Since we want an array of these devices to be paired with an array of detectors, beam deflection could lead to cross-talk between pixels. If the beam is deflected at a large enough angle with respect to the surface normal, it could internally reflect off the substrate/air interface, causing substrate modes that

propagate in the transverse direction. If we do not want any first-order diffraction in wavelengths longer than λ then the largest grating period, Λ, we are allowed is given by

$$\Lambda = \frac{\lambda}{n}, \tag{2.3}$$

where n is the refractive index of the substrate. We could also get reflective first-order diffraction, but since the index of the substrate is larger than that of air, it is the transmissive diffraction that places the upper limit on period [21].

Surface Plasmon Polaritons (SPP)

Surface plasmon polaritons (SPPs) are a type of electromagnetic wave that exists at the boundary of a metal and a dielectric. They can be explained by considering the effect of a plasma of free electrons in a metal. These oscillating electrons create an oscillating electric field in the neighboring dielectric. The coupled oscillations can propagate down the metal/dielectric interface with a wave number given by

$$k_{SPP} = \frac{2\pi}{\lambda}\sqrt{\frac{\epsilon_m \epsilon_d}{\epsilon_m + \epsilon_d}}, \tag{2.4}$$

where ϵ_m and ϵ_d are the relative permittivities of the metal and dielectric, and λ is the vacuum wavelength of light [22].

These oscillations are excited by the electric field of the incident light. In order for the excitation to occur, the electric field of the incident light must have a component that is normal to the interface since the tangential components would vanish [23]. We will see that SPP effects occur only for TM modes.

SPPs are highly sensitive to the boundary along which they propagate and are therefore useful in bio- and gas sensing [24]. An SPP can be observed indirectly via

an absorption line in the transmission and reflectance spectrum of the incident light, or directly by measuring the evanescent electric field at the interface.

We can also consider oscillations that occur in metal nanoparticles immersed in a dielectric, rather than a uniform metal/dielectric interface. These are referred to as localized surface plasmon polaritons (LSPPs) [25]. These can be used to confine electric fields to regions smaller than the wavelength of light.

We will see that LSPPs play an important role in the transmission characteristics of the devices by suppressing TM transmission at the SPP-resonant wavelengths, allowing us to shape the spectrum more effectively.

Rigorous Coupled-Wave Analysis (RCWA)

RCWA is a semi-analytic, Fourier-space computation method that represents periodic structures as a stack of layers that are periodic in the transverse directions and homogeneous in the direction of propagation. The permittivities can then be thought of as a periodic function in the tranverse coordinate. RCWA expands these functions in their Fourier components and inserts them into Maxwell's equations, which then solves them and gives us the mode shapes of the fields in each layer. The fields in each layer are related through boundary conditions. The user-input initial condition in the input region can then be propagated through the device to the output region [26–29]. Figure 2.3 shows how our device can be represented as three layers: 1) gold-air, 2) dielectric-air, 3) dielectric-gold.

The MATLAB code used for these simulations was developed by Dr. Vincent Paeder [30]. Large simulations were made possible by the Hyalite Research Computing Cluster at Montana State University [31].

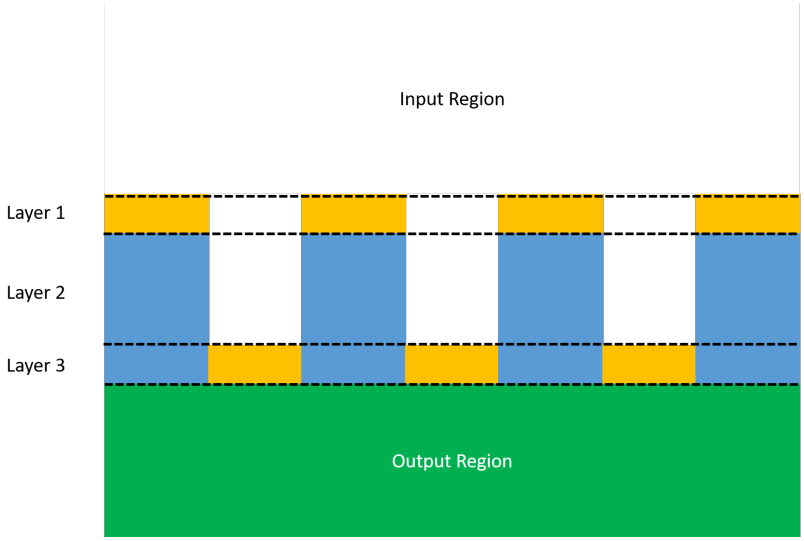


Figure 2.3: To use RCWA, we take the one dimensional grating and separate it into layers or regions that are periodic in the transverse direction but homogeneous in the direction of propagation.

Fabry-Perot Resonance (FP)

FP resonance between gratings

A resonance occurs in the cavity between the two gratings in Figure 2.1 when the FP condition equation is met,

$$\phi_{r_{21}} + \phi_{r_{23}} + \frac{4d_2 n_{eff}\pi}{\lambda} = m2\pi \tag{2.5}$$

where $\phi_{r_{21}}$, $\phi_{r_{23}}$ are the phases accrued upon reflection from top and bottom interfaces surrounding Region 2, respectively, d_2 is the separation of the gratings described in Figure 2.1, n_{eff} is the effective index of Region 2, λ is the vacuum wavelength of light incident on the grating, and m is an integer [32]. The subscripts of the phase terms, ϕ_{ij}, refer to the reflection from the ith region off the interface with the jth region.

To understand what $\phi_{r_{21}}$ and $\phi_{r_{23}}$ would be, we can take typical values of n_1 and n_2 and calculate the effective indices for the TM and TE cases for different fill factors. Figures 2.4 and 2.5 show that, for the TM case, (1) all three layers can be treated as dielectrics (except for extreme values of fill factor), and (2) Region 2 is less optically dense than the surrounding layers. Since waves reflecting off of a more optically dense material undergo a sign flip, we can make the reasonable approximation that $\phi_{r_{21}} = \phi_{r_{23}} = \pi$. We can do a similar analysis for the TE case: Figures 2.6 and 2.7 show that while Region 2 is still a dielectric, the surrounding layers are effectively conductive. Waves reflecting off metallic surfaces also undergo a change in sign, so the approximation that $\phi_{r_{12}} = \phi_{r_{23}} = \pi$ remains valid for the TE case.

By making the proper substitutions into Equation 2.5 and by choosing a mode index $m \to m + 1$, we obtain the following formula for the FP peak wavelengths:

$$\lambda_{FP} = \frac{d_2 n_{eff}}{m}, \tag{2.6}$$

where n_{neff} is polarization dependent.

Figure 2.8 uses Equation 2.6 to plot the positions of the FP peak for changing grating separation and mode number. To achieve a first-order FP peak at 2 μm, a grating fill factor 0.5 must have a grating separation of 800 nm. A second-order resonance would occur at the same wavelength if the grating gap was increased to 1.6 μm. Exact simulation results show remarkably good agreement with the theoretical predictions, Figures 2.9 and 2.10. A major difference between simulation results and EMT and 2.8 is the presence of an FP resonance that occurs at grating gaps lower than the first-order FP resonance in the TM case in Figure 2.9. This is caused by a resonance in the top layer of gold itself. The TE case shows much better

agreement with theory since the dielectric-in-metal resonator is valid regardless of grating separation.

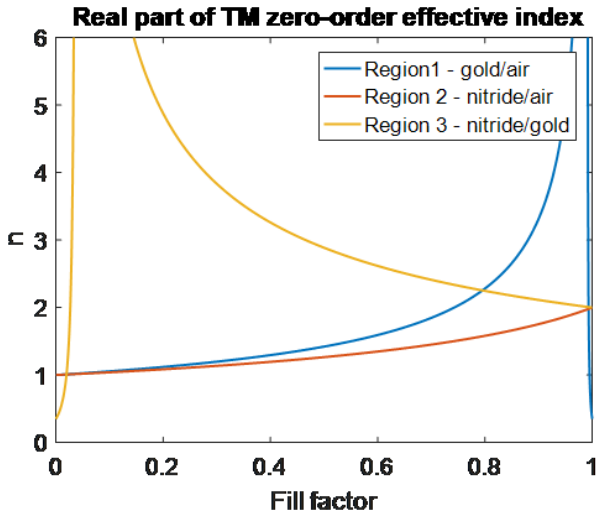


Figure 2.4: Real part of TM effective index of refraction for each layer of device as a function of fill factor. Cavity between metal gratings has the lowest index. $n_1 = 2$ and $n_2 = 1.47$

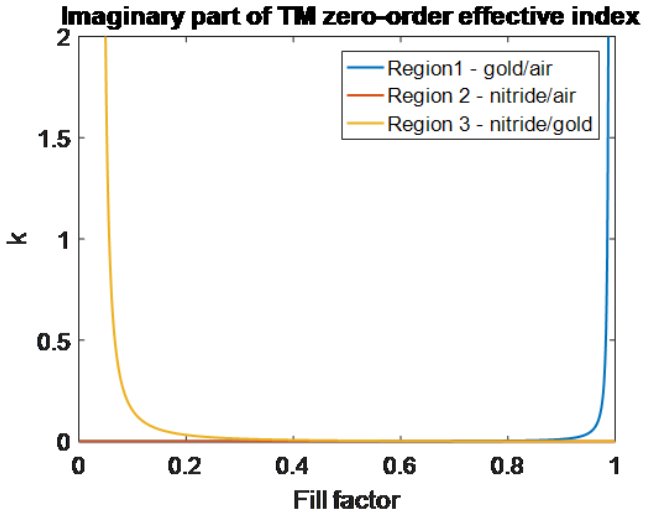


Figure 2.5: Imaginary part of TM effective index of refraction for each layer of device as a function of fill factor. This shows that each layer can be approximated as a lossless dielectric for the TM case except for extreme values of fill factor. $n_1 = 2$ and $n_2 = 1.47$

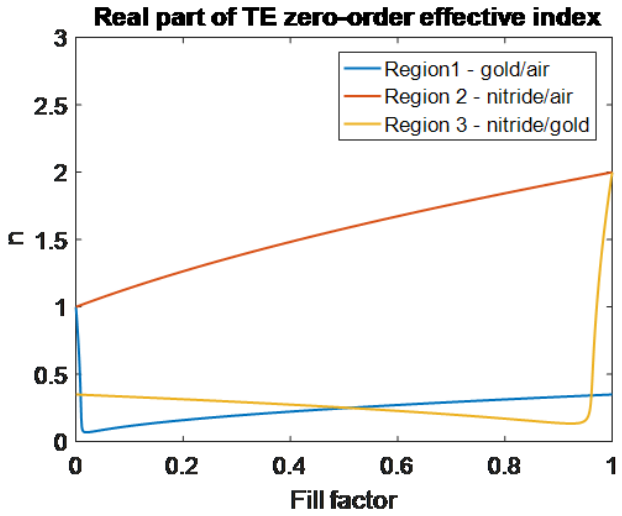


Figure 2.6: Real part of TE effective index of refraction for each layer of device as a function of fill factor. $n_1 = 2$ and $n_2 = 1.47$

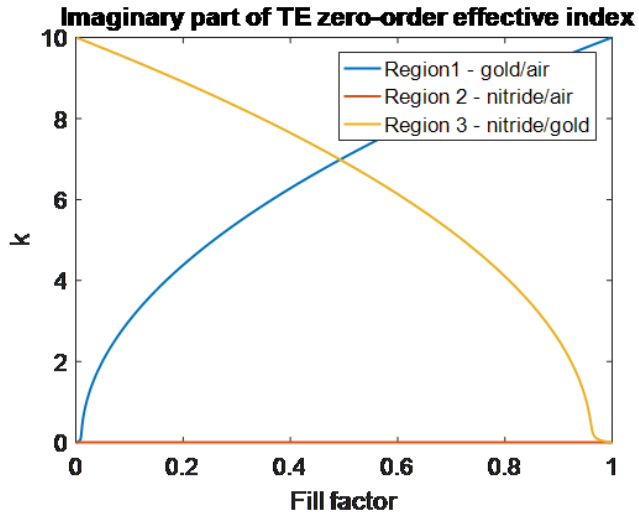


Figure 2.7: Imaginary part of TE effective index of refraction for each layer of device as a function of fill factor. For Regions 1 and 3, it is larger than the real part, indicating metallic behavior. $n_1 = 2$ and $n_2 = 1.47$

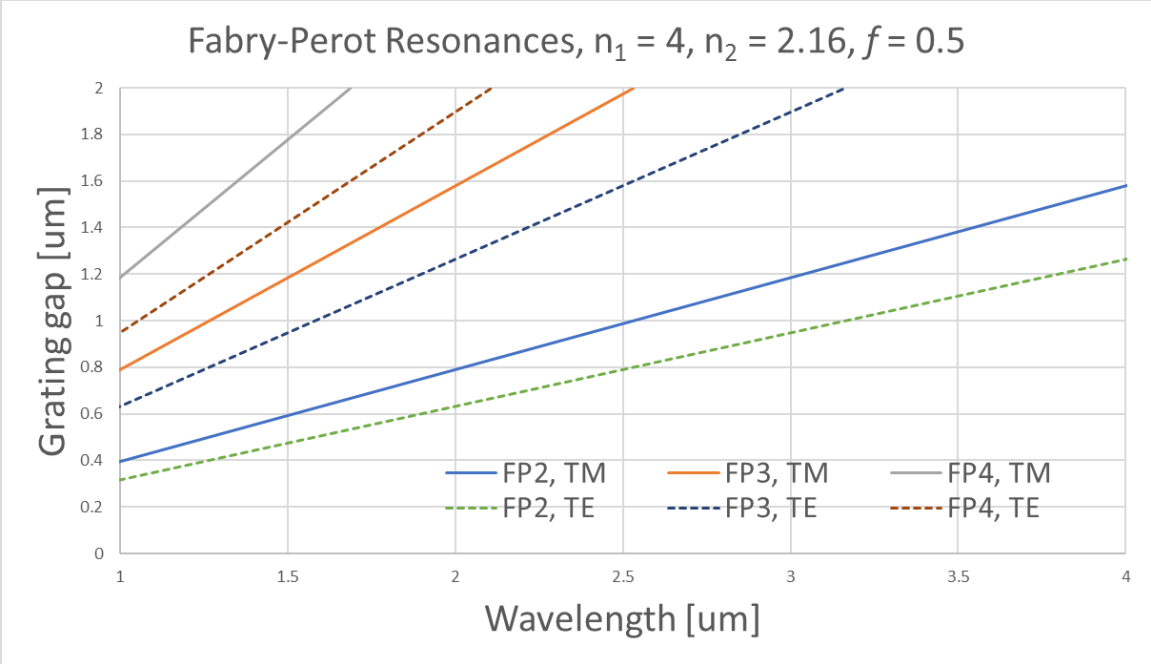


Figure 2.8: Plot of the positions of the FP peak wavelengths with changing grating gap and mode number. Fill factor f is 0.5, $n_1 = 2$, $n_2 = 1.47$

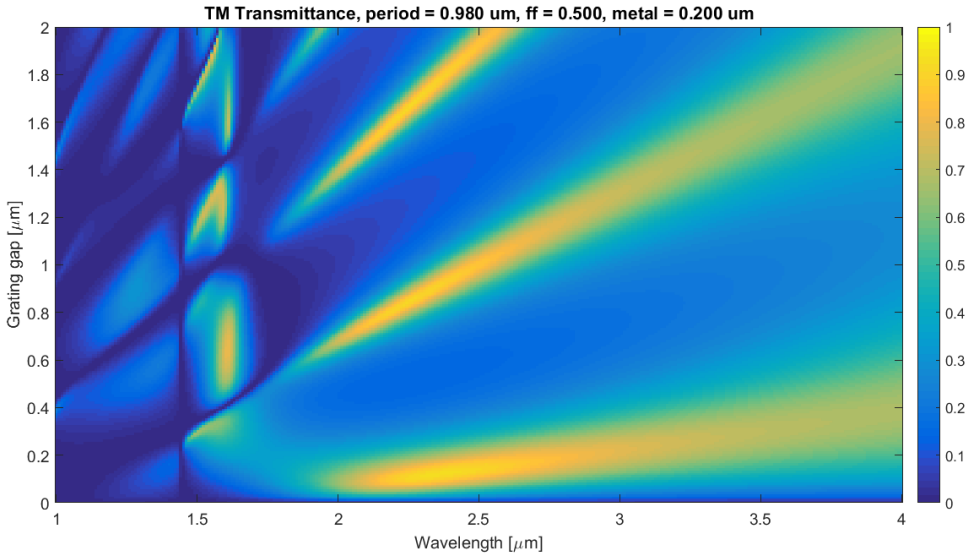


Figure 2.9: RCWA simulations showing TM transmittance as a function of grating separation and wavelength. The presence of a first order resonance is not surprising since the single dominant dielectric cavity approximation is not valid for such small grating separations $\Lambda = 980$ nm, $f = 0.5$, $n_1 = 2$, $n_2 = 1.47$, and $d_1 = 200$ nm

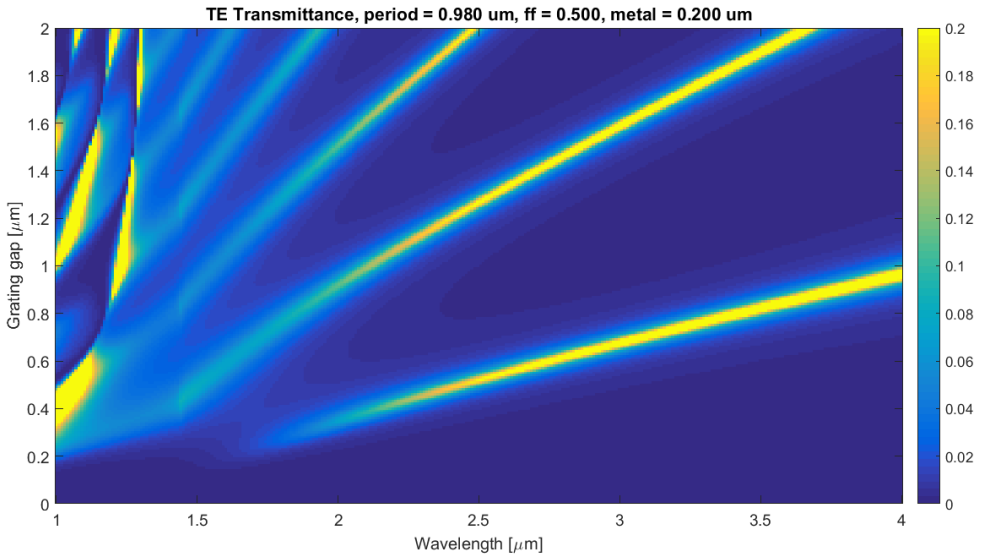


Figure 2.10: RCWA simulations showing TE transmittance as a function of grating separation and wavelength. This shows much better agreement with Figure 2.8 than does Figure 2.9. $\Lambda = 980$ nm, $f = 0.5$, $n_1 = 2$, $n_2 = 1.47$, and $d_1 = 200$ nm

One important feature of Figure 2.9 is that the spectral full-width half-max (FWHM) decreases as mode number increases. This a result of plotting the spectrum in wavelength space. In frequency space, the spectral widths would remain constant and depend mainly on the finesse of the cavity. Highly reflective mirrors produce very narrow FWHM. The boundaries of our devices had a low dielectric contrast, making them poorly reflective, and therefore low-finesse. This presented a fundamental problem in having the wavelength selectivity come solely from the FP resonance.

FP Resonance in Bottom Layer

From Figure 2.4 it can be seen that the effective index of Region 3 is much higher than the indices of the other two regions for lower fill factors. At such low fill factors it would become much easier to excite resonant modes in Region 3, which would be

problematic. Luckily, for high TE rejection, we tend to want larger fill factors so this doesn't end up being a problem in practice.

TM Transmission Minima at SPP Excitation Frequencies

The geometry of our device allows for the presence of SPPs at two different interfaces that we can exploit to improve performance. Figure 2.11 describes where these SPPs would exist. We want to utilize SPP resonances because Cao et al [33]

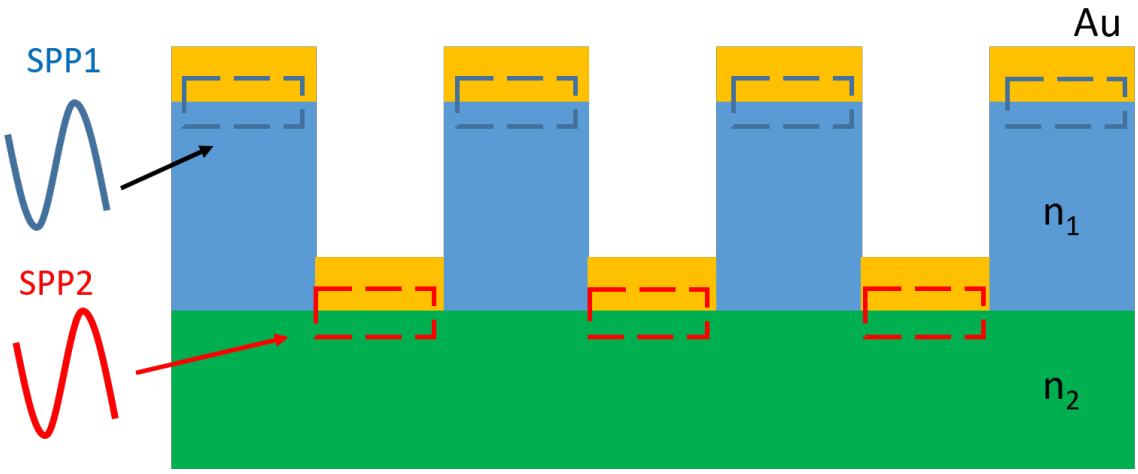


Figure 2.11: Two different metal-dielectric interfaces allow for the presence of two different SPP resonances (SPP1 and SPP2). SPP1 exists at the interface between the top gold grating and n_1 while SPP2 exists at the interface between the bottom gold grating and n_2.

found that a TM transmission null occurs when the SPP wavelength matches the period of the grating. This occurs even at zero incidence angle. This is useful because it allows us to engineer the shape of the bandpass by strategically placing these resonances on one or both sides of a FP resonance.

A log plot of the TM transmittance (Figure 2.12) allows us to see the null points much better. One null point lies at roughly 1.5 μm. This null is independent of grating separation and corresponds to the bottom substrate/gold interface. The second null

point corresponds to the top dielectric/gold interface and is certainly not independent of grating separation since it sees an effective index of the middle region.

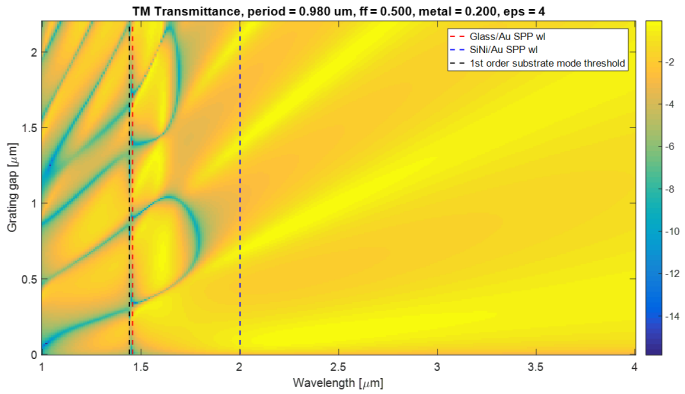


Figure 2.12: Log plot of TM transmission as a function of grating gap and wavelength. A null corresponding to the glass/Au SPP wavelength occurs exactly where it is predicted and is independent of grating gap. The null corresponding to the silicon nitride/Au interface depends on the grating gap since it sees an effective index of the middle region.

SPP/FP Coupling

Away from any SPP resonance, the fields are highly confined to the air between the dielectric pillars (Figure 2.13). Close to the SPP resonance of the top gold/dielectric interface, more of the field is localized in the dielectric pillars (2.14). This raises the effective index of Region 2. If the effective index then exceeds the effective index of Region 1, then waves reflecting off that interface back into the device will no longer undergo a 180-degree phase shift, so $\phi_{r_{21}} = 0$. In this regime the condition for FP resonance changes from Equation 2.6 to become

$$\lambda_{FP} = \frac{d_2 n_{eff}}{m - \frac{1}{2}}. \tag{2.7}$$

Figure 2.15 shows simulation results that confirm this behavior. Once an FP resonant peak crosses the threshold of the top gold/dielectric SPP resonance, it becomes an anti-FP resonance with a new resonance appearing where the ant-FP resonance would have been in the absence of an SPP resonance. This new resonance also appears to be largely independent of grating separation.

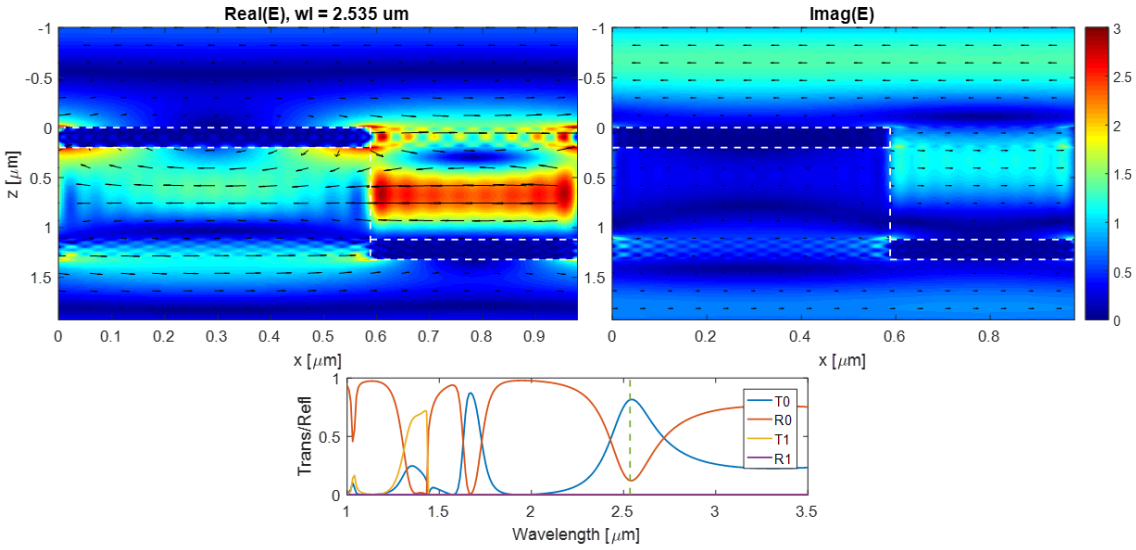


Figure 2.13: Top figures show the electric field strength of a normal FP resonance, that is, one that is far from an SPP resonance. The field is highly localized in the air gap. The bottom plot shows transmission as a function of wavelength.

Conclusion

I used theory and numerical simulation to explain the qualitative behavior of the two-layer subwavelength gratings when illuminated with both TE and TM light.

I have confirmed that an FP resonance occurs in the cavity between the two gratings both for TM and TE polarizations. For TE polarization, most of the energy is rejected at the initial air/grating interface. For TM polarization, the initial interface

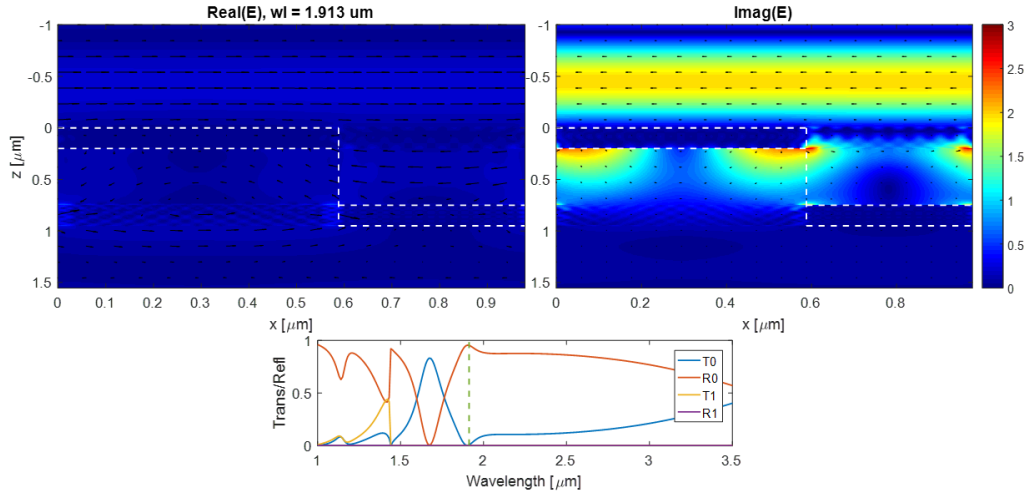


Figure 2.14: Near SPP resonance, the field becomes more localized in dielectric pillars raising the effective index of the middle region.

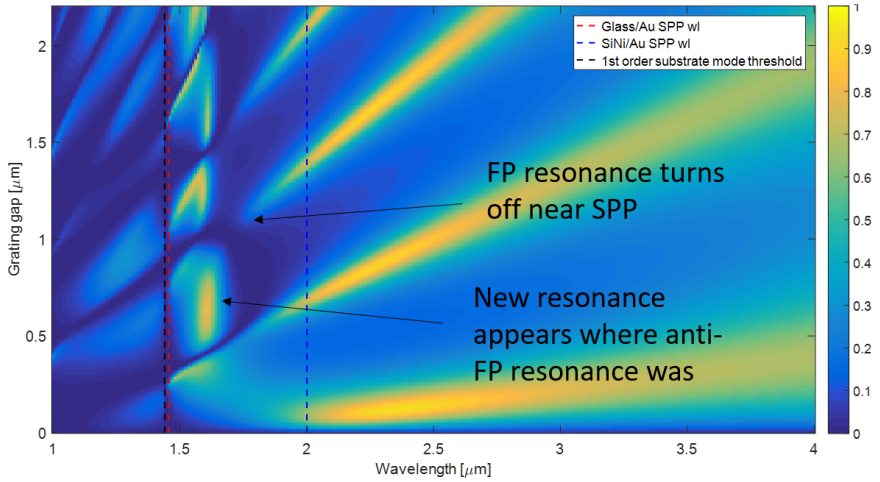


Figure 2.15: FP resonance turns off and new resonance appears where anti-FP resonance would be in the absence of an SPP

appears as an effective dielectric, resulting in stronger fields in the cavity. High transmission occurs at TM resonant wavelengths.

I went on to demonstrate that, though we get a definite resonance in between the cavity, its quality factor is low due to the low dielectric contrast at the interfaces inside the cavity. This results in a broad spectrum with high out-of-band transmission on the longer wavelength side of the passband. This problem was fixed by placing the null points caused by SPP excitation on either side of the FP peak. Not only did this improve the out-of-band performance of the device, but the proximity of the FP peak to the SPP resonances caused its behavior to change, resulting in a narrower and higher passband.

I have shown that this geometry is capable of meeting the two requirements for the three-channel, polarization selective Bayer filter: (1) high TE mode rejection caused by the subwavelength grating geometry, and (2) highly selective TM transmission that is caused by the coupling between the FP and SPP resonances.

CHARACTERIZATION AND MODEL IMPROVEMENT

Overview

An important requirement of these spectral bandpass filters is the ability to tune their peak TM transmission wavelength to a specific wavelength band. Before we begin the design process in earnest we need to ascertain any unaccounted-for deviations from the simulation model and reality.

In this section I show how a discrepancy of peak transmission wavelength between an early fabricated device and simulation can be accounted for by taking into account the narrowing of the silicon pillars and by adjusting the gold material properties. The results of these experiments also showed us that we can use separate fill factors for both silicon and gold.

Background

Preliminary Design

Before the design process began, we fabricated a proof-of-concept device that would demonstrate how, if we separated the two gold gratings by a larger distance than the original polarizing beam splitter device, we would get a sharper TM response due to a higher order FP resonance. This device wouldn't have good enough spectral performance or polarization selectivity to serve as the final device, but was used to be an early comparison between simulation and experiment.

Fabrication

Silicon chips were coated with two layers of resist. Our grating patterns were then transferred onto the top layer of resist using electron-beam lithography. Exposed resist was then dissolved away, after which the now exposed bottom layer of resist

was dissolved away. This left an undercut trench with bare silicon at the bottom. We then deposited a 20-nm layer of aluminum onto the chips, then dissolved away the remaining resist. This left an aluminum negative of the desired grating pattern on the chip that would act as an etch mask. Once the chips were etched, the aluminum was removed and a layer of gold was deposited.

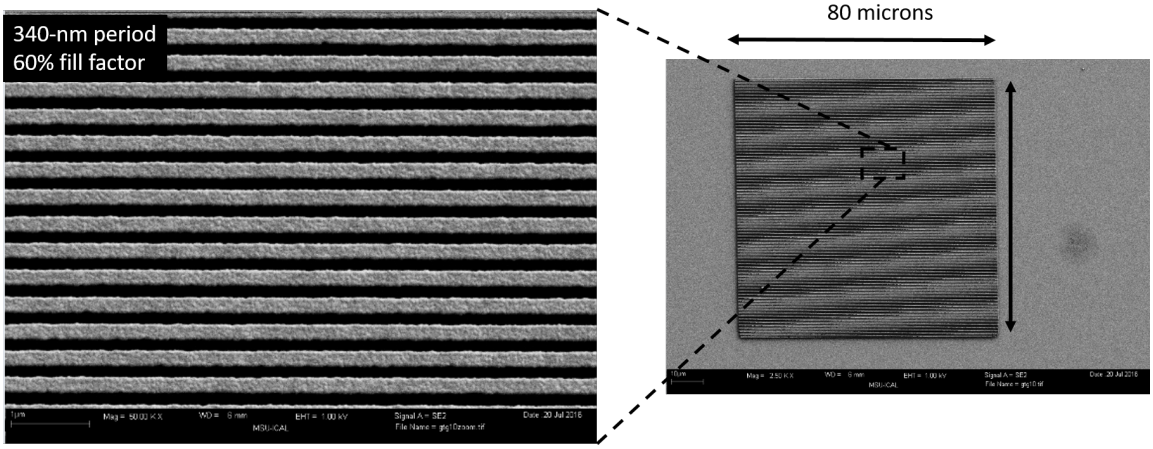


Figure 3.1: An SEM image of a completed 80-micron by 80-micron grating. The period is 340 nm and the fill factor is 60%.

White Light Spectral Test System

We optically characterized our devices (Figure 3.2) by illuminating them with pseudo-collimated white light (1 to 2.5 microns) from a fiber-coupled halogen source (Mikropack HL-2000). We then magnified the image of the array of polarizers so that we could select the output from only one device using an aperture. The transmitted light was then passed through an analyzing polarizer before being imaged into a fiber coupled spectrometer (ASD FieldSpec Pro).

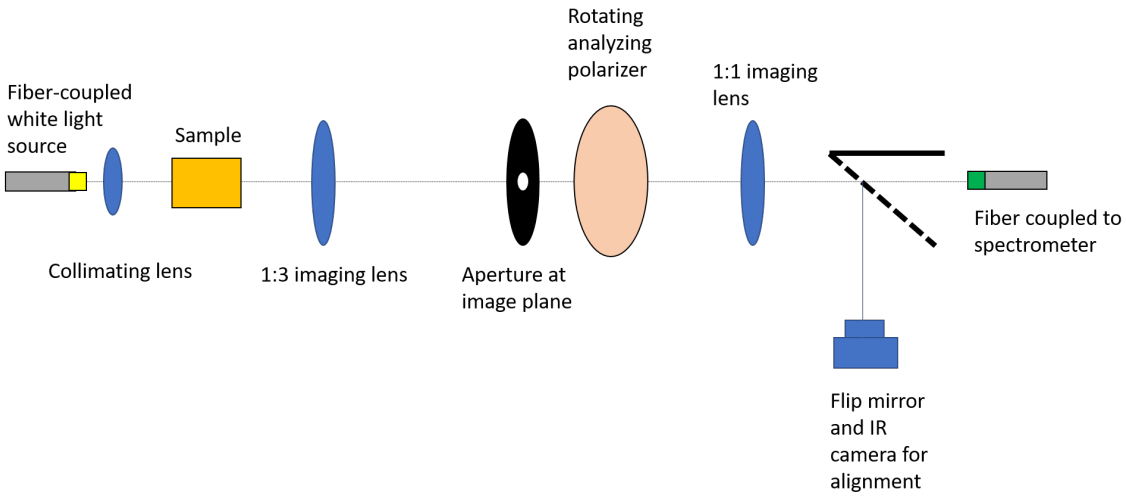


Figure 3.2: Devices were illuminated with white light. Transmitted light was passed through an analyzing polarizer before being imaged into a fiber coupled spectrometer.

Comparison of Simulation to Test Results

Results of experiments (Figure 3.3) show a spectrum that is very similar to simulations but shifted by roughly 300 nm. The shift occurs not only for the peak of the FP resonance, but also for the null point, though is difficult to measure precisely since the null point wavelength in the experimental data is lower than the wavelength where silicon stops being transparent.

Improvement to Model

In order to use experimental results for improving our simulation models, we had to determine the source of the discrepancy.

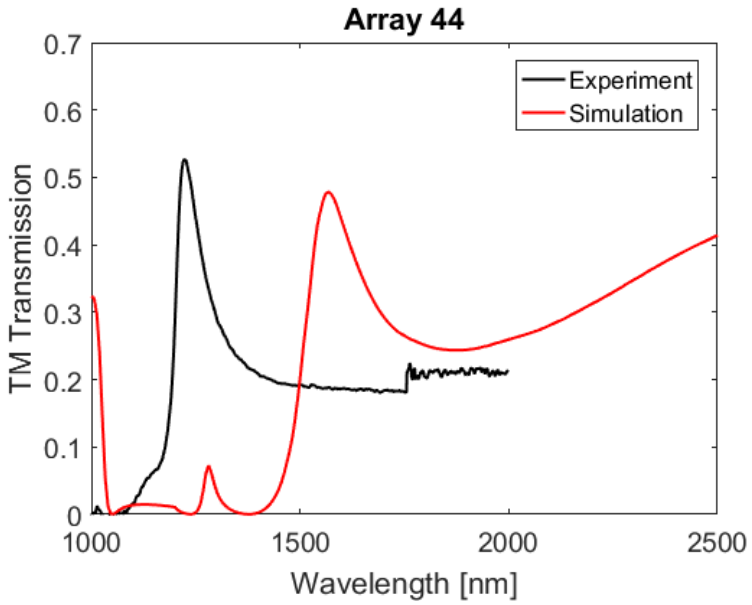


Figure 3.3: Experimental results of a device show an offset in the spectrum of roughly 300 nm. Both the peak and the null point are shifted by the same amount.

Material Properties

Dispersive dielectric functions were taken from literature and used in our RCWA models [34–38]. The dielectric constants for gold and silicon are roughly near $-100+7i$ and 12.25, respectively.

Gold Dielectric Function The dielectric function of gold in the shortwave infrared region differs greatly from study to study, as is seen in 3.4. At a wavelength of 1.6 microns, the real part of the dielectric varies from -100 to almost -200, a change of 100%. The imaginary part also varies quite a bit, but simulations show that the imaginary part had little effect on the location of the spectral peak. Variation of the real part definitely had a slight effect, suggesting that gold material properties could be partly responsible for the discrepancy.

One source of this variance is that the optical properties of thin films depend greatly on the matter in which they were deposited [34].

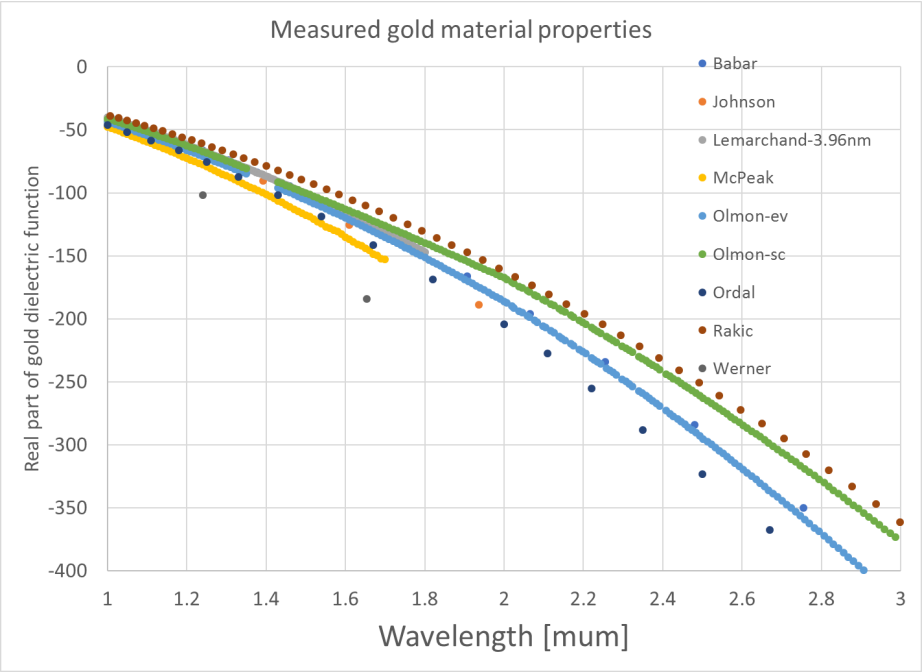


Figure 3.4: This figure shows that large range of measured dispersion curves for gold in the near infrared region. [34–38].

Silicon Dielectric Function Contrary to the gold material properties, the material properties of bulk silicon are very well known and don't vary much at all between studies (Figure 3.5) [39–42].

Geometry

The fact that altering the silicon optical properties had such a drastic effect on device performance suggested that unintended device geometries were responsible for the discrepancy between experiment and simulation. Etch profiles did indeed show silicon pillars that were not square, but narrower in the middle than they were at the top and bottom. From Figure 3.8 we can see that the width of the silicon pillar in the middle was about 60% of that of the gold ruling. In simulation, the top gold ruling width was assumed to be complementary of the width of the bottom gold ruling (meaning their sum is the period of the grating). A deviation from that assumption

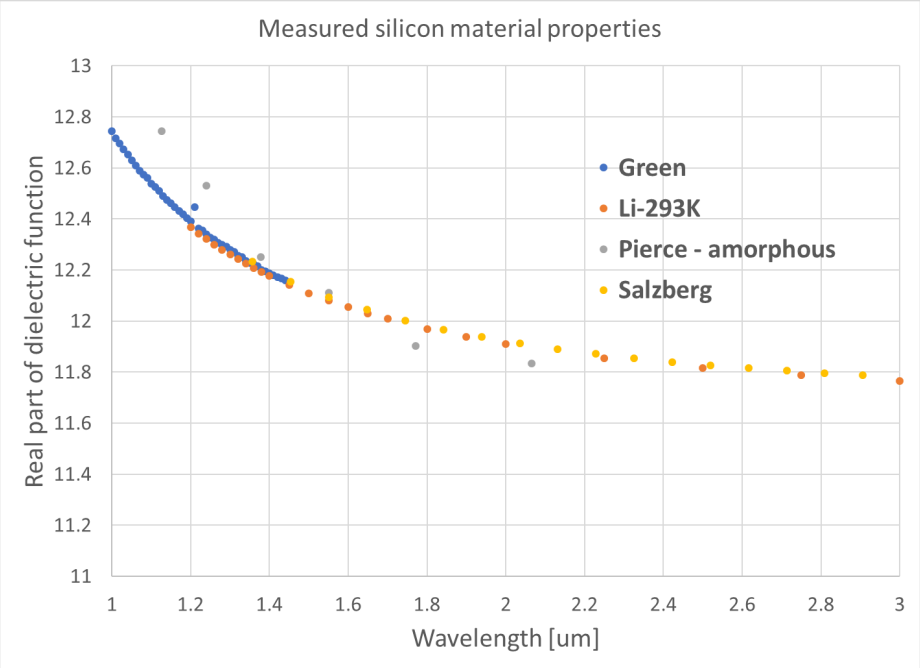


Figure 3.5: Silicon, unlike gold, has material properties that do not change much. In this figure, the only outlier was amorphous silicon, which is not used in this device [39–42].

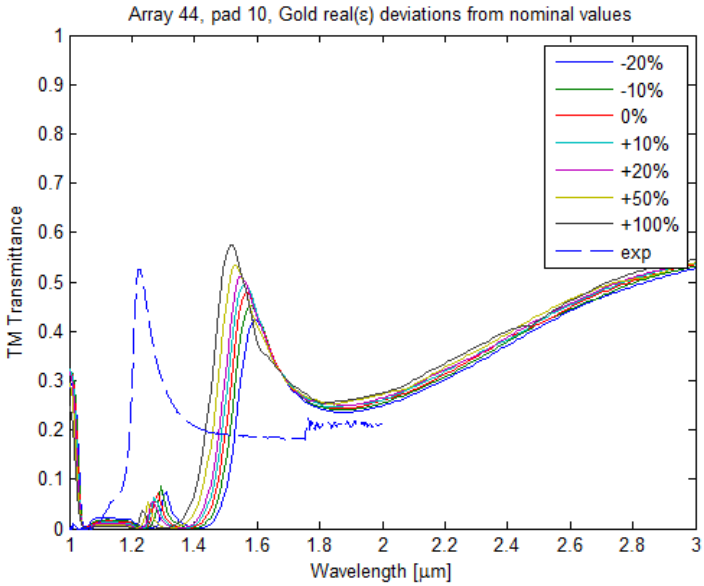


Figure 3.6: Altering the real part of the gold dielectric function indeed had an effect on the wavelength of peak TM response.

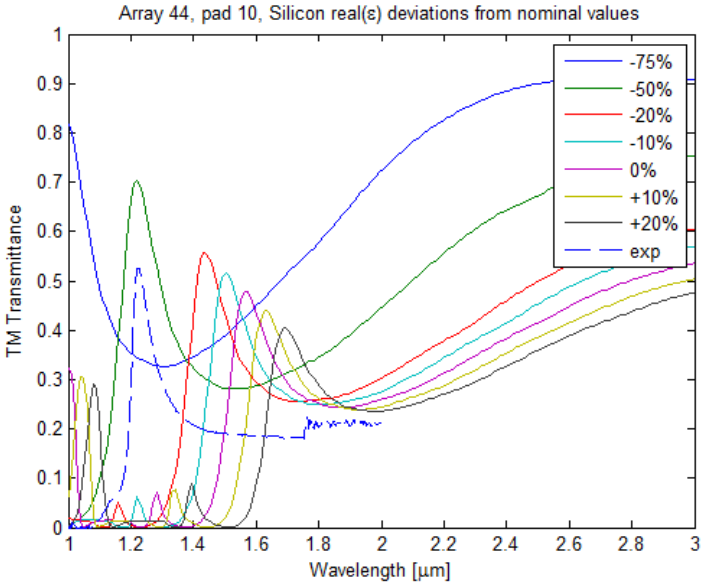


Figure 3.7: Altering the silicon dielectric function had an overwhelming effect on the wavelength of peak TM response. While the possibility of the bulk silicon properties themselves having changed was extremely unlikely (Figure 3.5), it did raise the possibility that imperfections in the geometry of the grating could be responsible.

would affect device performance, but there did not seem to be any sign of that in Figure 3.8. If the filling between the gold gratings had a lower effective index of refraction, then the effect would be similar to lowering the bulk silicon index, as in Figure 3.7.

To confirm this, simulations were run that approximated this narrowing of the silicon pillars (Figure 3.9). The spectra was blue shifted for narrower periods. This makes sense if you think of the resonant cavity between the metallic being filled with a dielectric. By reducing the size of the waist of the pillars, you are lowering the effective index of that dielectric, which would result in a blue shift of the resonant wavelength (Figure 3.10). Simulating the devices with a narrow waist required much more simulation time since it requires more layers to approximate (seven layers in

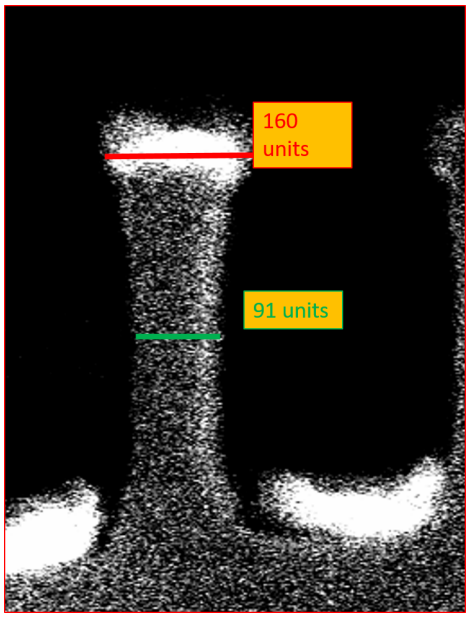


Figure 3.8: Image of a cross section of a grating taken with an SEM shows that the middle of the silicon pillar was about 60% as wide as the top gold ruling.

Figure 3.9). The same result was achieved by treating the dielectric as having a smaller fill factor than the gold grating (Figure 3.11).

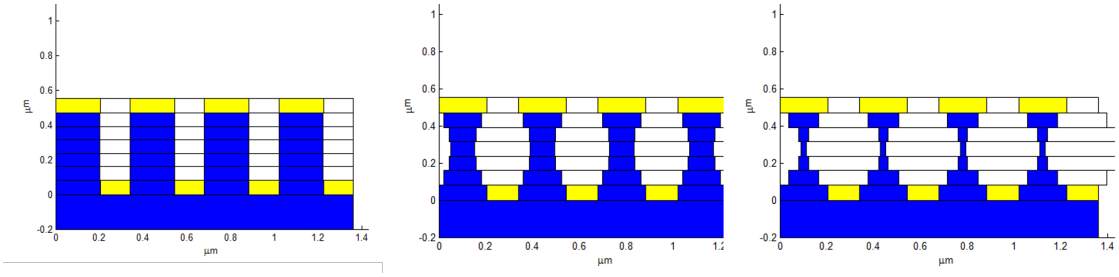


Figure 3.9: Examples of device geometries used to investigate the effect of narrow silicon pillars on device performance.

When we adjusted the real part of the gold dielectric function to be 100% larger (more negative) and adjusted the silicon fill factor to account for the undercut, the experimental results matched the simulation results much more closely (Figures 3.12 and 3.13).

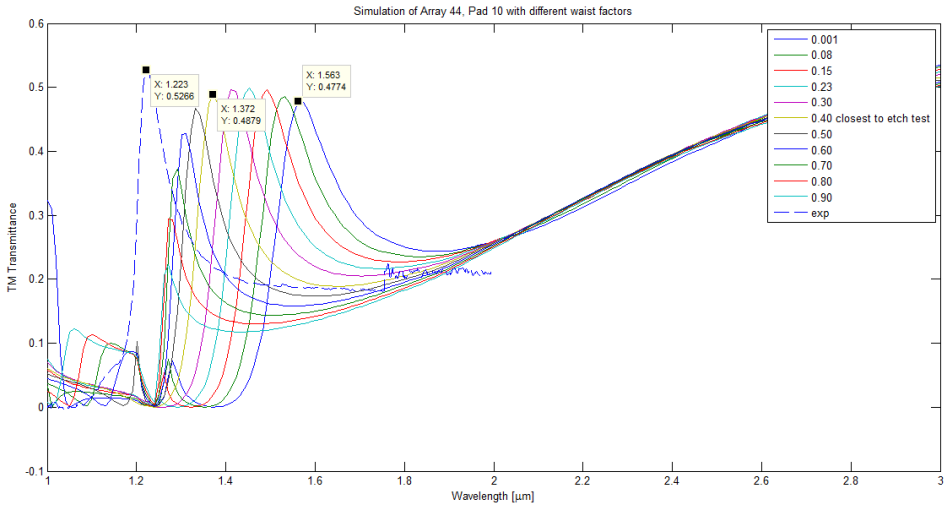


Figure 3.10: Increasing the narrowness of the silicon pillars blue shifted the spectrum.

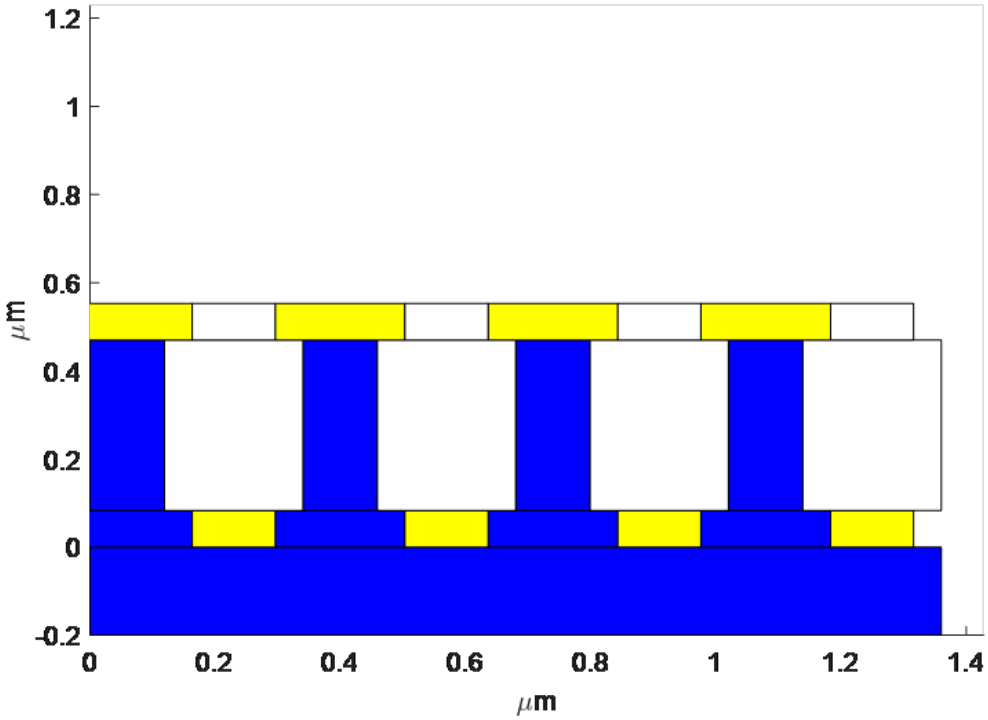


Figure 3.11: It is sufficient to approximate pillar narrowness by using a separate fill factor for silicon than for gold. Since this is a three layer device, we don't have the increase in the simulation time that a 7-layer device would have.

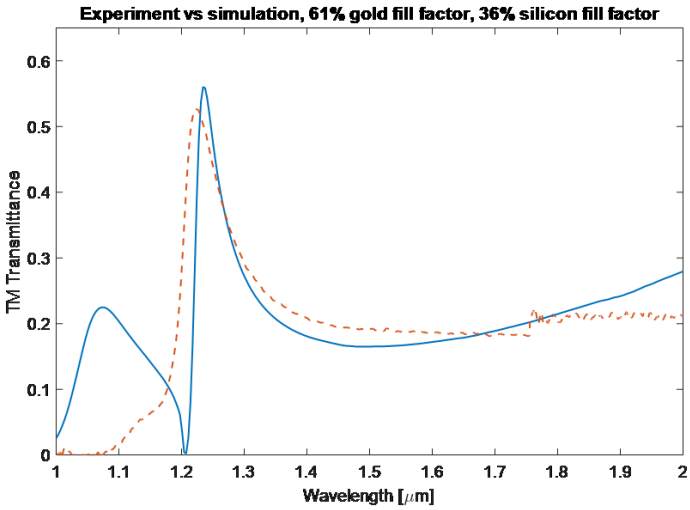


Figure 3.12: Discrepancy resolved from using a realistic silicon fill factor and increasing the real part of the gold dielectric by roughly 100%.

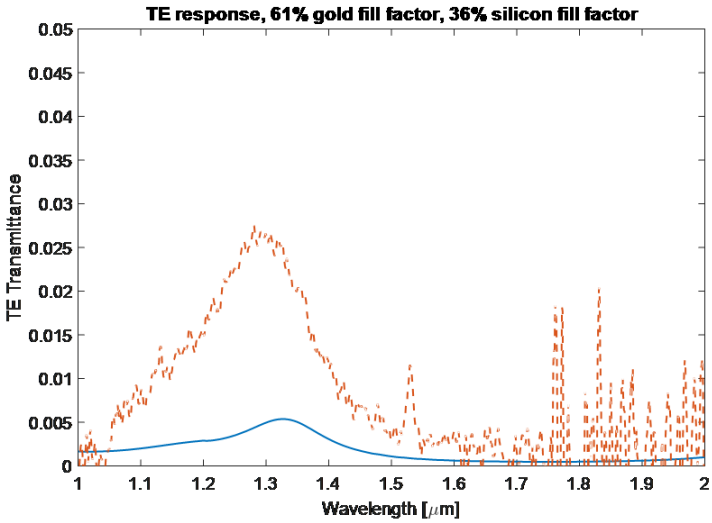


Figure 3.13: The TE response peaks roughly correspond to each other after the correct silicon fill factor and higher gold dielectrics are used.

Discrepancy Between Experiment and Simulation from Parameter Tolerances

While the largest sources of the offset between simulation and experiment were found to be gold material properties and non-square grating geometry, fabrication tolerances in the device parameters could also have led to shifts in the peak transmission wavelengths.

Grating Separation Since the position of the FP peak is most strongly coupled to the size of the resonant cavity, any uncertainty in the etch depth could contribute significantly to the discrepancy. Figure 3.14 shows how under-etching the devices could shift the spectrum to be more in line with experiment. However, even at a significant deviation of 20%, the discrepancy was not resolved and the device performance was greatly degraded suggesting this parameter could not be solely responsible.

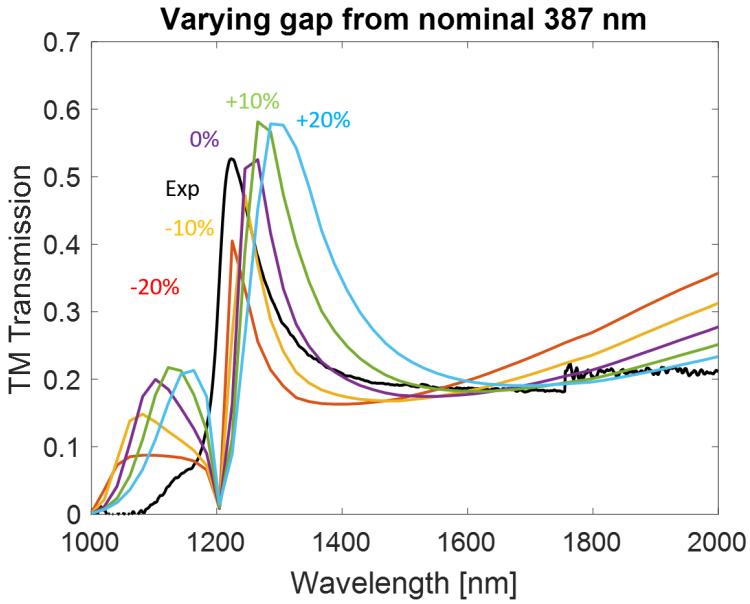


Figure 3.14: Deviations from intended grating separations do indeed result in the wavelength shifting of the spectrum, but it is also accompanied by a reduction in performance, and the shift is not enough to account for the entire discrepancy.

Fill Factor Similar to grating period, fill factor is a parameter that we can easily measure, so is unlikely to be responsible for the discrepancy. Figure 3.15 shows that fill factor still has the ability to shift the spectrum.

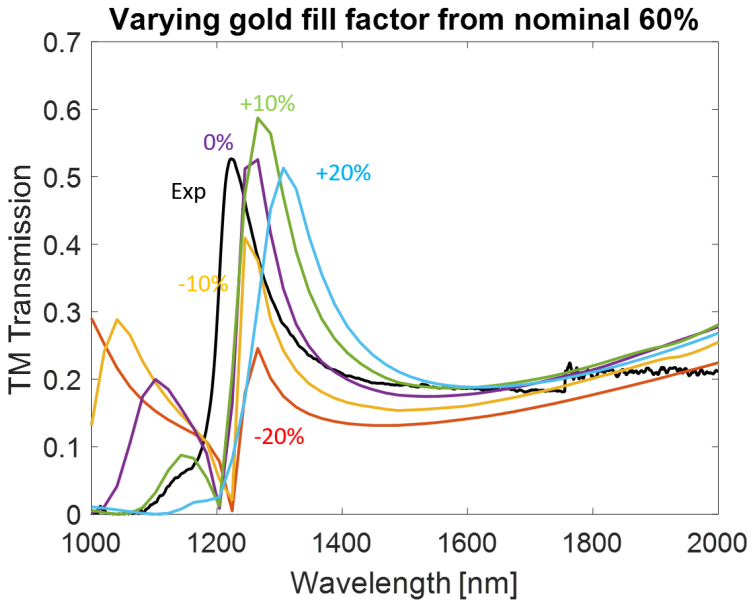


Figure 3.15: Similar to period, fill factor is something that can shift the response, but is known to a higher accuracy than etch or gold depth since it is measured for each device.

Gold Depth Gold depth is very weakly coupled to the position of the spectra, as is seen in Figure 3.16.

Conclusion

We were able to fabricate wavelength-selective polarizers out of gold and bulk silicon and test them using the white light spectral characterization set-up.

The discrepancy between experiment and simulation can be accounted for by including the non-square silicon grating structure and by allowing the gold material properties to vary in a manner that is consistent with literature. I have shown

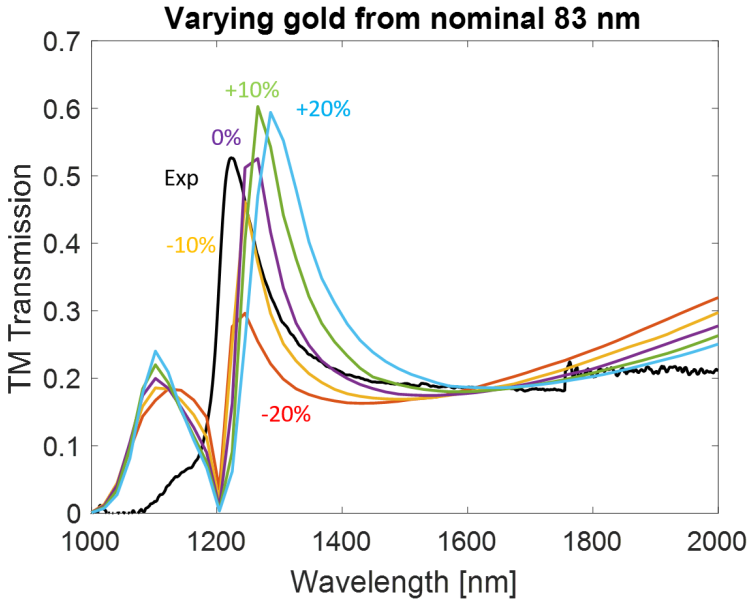


Figure 3.16: Altering the gold depth has little shifting effect and so cannot be the source of the discrepancy.

that slight discrepancies can also be accounted for with fabrication tolerances in period, fill factor, and gold depth, but these are relatively minor. Understanding how these imperfections affect device performance is critically importance since the project depends on being able to accurately place the peak response of a filter at 1640 and 1700 nm, a difference of only 60 nm.

I validated the corrections made to the simulation by comparing updated simulation results to experiment for a different grating that had a much broader spectral response. While the experimental results didn't show as high a peak as we were expecting, the null point at for both simulation and experiment both landed on 1100 nm. Since the lower transmission could be accounted for by imperfections in the grating, I took this to be an indication that the improvements to the simulation model are valid.

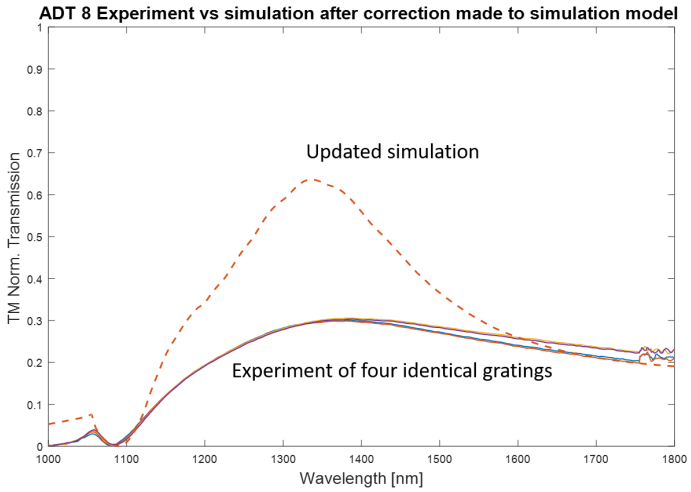


Figure 3.17: Here is a comparison between measurement and simulation (with model improvements) for a grating that had a much broader spectral response. Although the absolute transmission levels didn't match, the null points at 1100 nm matched quite well. The reduced transmission could be explained by imperfections in the gratings.

Not only was it important to learn the effects of non-ideal geometry and material properties on device performance, but it gave us the insight to include the narrowness of the silicon pillars as a design parameter. Because of fabrication concerns, up to this point, the silicon and gold fill factors have been the same, despite the fact that the gold grating and the dielectric grating have been the same.

I would like to take the opportunity to thank the following people for their work in carrying out a large part of the fabrication work for these devices: Carol Baumbauer, Orrin Boese, James Dilts. I would also like to thank Benjamin Moon and Tristan Gray for optimizing the white light characterization set-up and for taking a majority of the data.

SILICON DEVICE DESIGN

Overview

This chapter discusses the design procedure for a polarization-selective bandpass filter using a silicon-on-quartz design. The result is a device optimized for operation at 1550 nm with a passband of 100 nm, a vast improvement over previous silicon-only devices.

Introduction

This device was to consist of a surface relief grating fabricated on a silicon coated quartz wafer. The period, fill factor, grating gap, and gold depth were to be the parameters that would be tuned to create the desired performance.

A naive approach to choosing the device parameters would be to vary each parameter independently and in parallel. This approach, however, is resource intensive. The results could also be vastly different depending on how we weight a merit function. Since, at the time of design, it was not known how important each filter property (peak transmission, FWHM) would be for the ultimate application, a more theoretical approach to design was taken.

Period and Silicon Fill Factor

The period of the grating predominantly affects two things: the existence of first-order diffraction orders, and the wavelengths of SPP excitation. The procedure began with locating our anchor points. To do this I plotted the resonant wavelength for the SPP at both interfaces as a function of period. On the same plot, we show the desired location for our anchor points. The anchor points were centered around 1550 nm and were 400 nm apart from each other. This separation was chosen because we

would like them to be as close together as possible, but if we put them closer together, a sufficiently strong FP peak would not appear between them.

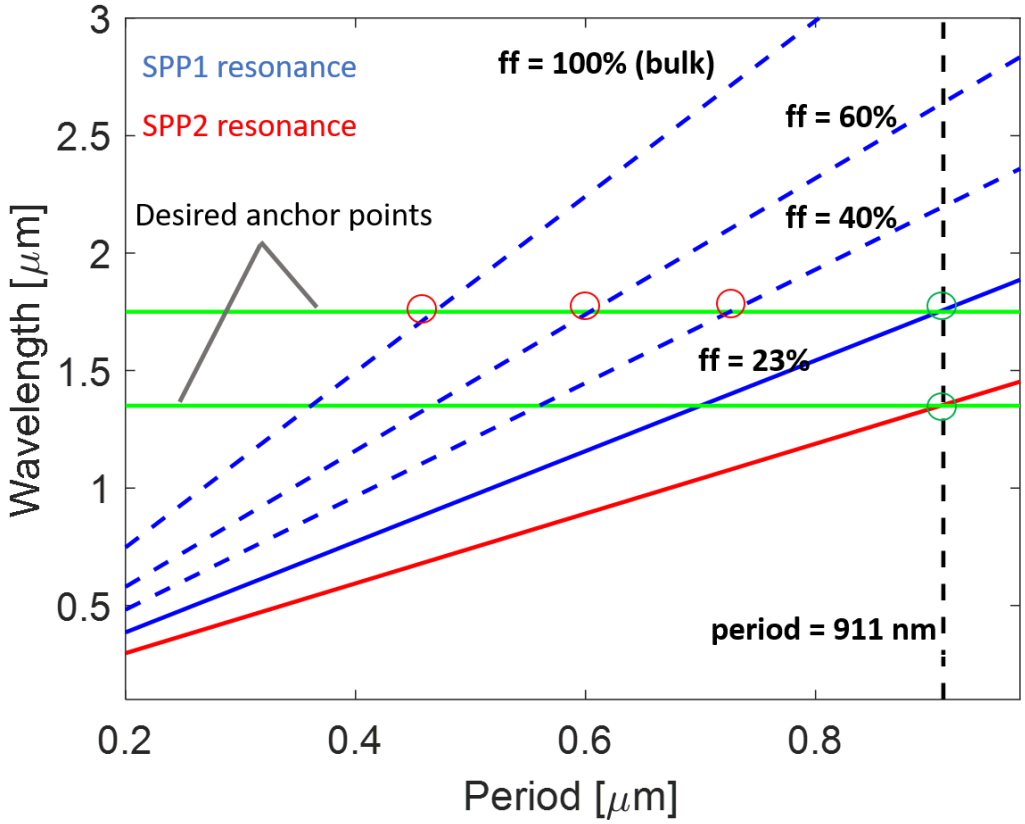


Figure 4.1: The silicon fill factor and period of the grating are chosen by requiring that the anchor points must be symmetric around the design wavelength. We are looking at the points where the bottom SPP resonance intersects the lower anchor wavelength, and where the top SPP resonance intersects the upper anchor wavelength. This only occurs at a fill factor of 23% and at a period of 911 nm.

We needed to bring the resonances closer together before we could determine a period value. Since we were trying to make these devices using silicon on glass, we could not alter the refractive index of the filling material. However, we could take advantage of the fact that the effective index of the middle material will change with silicon fill factor. By reducing the silicon fill factor we could see the resonances being

brought closer together. At a fill factor of about 23%, the top SPP curve intersects the top anchor point and the bottom SPP curve intersects the bottom anchor point at the same period of 911 nm.

Grating Separation, Gold Fill Factor, and Gold Depth

Once we had determined the positions of our anchor points by selecting period and silicon fill factor, we wanted to tune the resonance within the cavity so that it appeared between the anchor points. This was not a purely FP resonance, so a precise starting point was more difficult.

Simulations were run for a wide range of gaps, ranging from 200 nm to 750 nm. From the logarithmic plot, one can see that the null points caused by SPP resonance occurred roughly at their predicted wavelengths (Figure 4.2). At small gaps values, the top resonance started to shift, which is understandable since we'll have a large change in effective index due to stronger field coupling within the grating. For shorter wavelengths, the null points became more complex. This is due partly to higher order SPP resonances, but we are not concerned with it since it is outside our band of interest.

The linear plot of TM transmission showed a very sharp maximum that is apparently independent of etch depth (Figure 4.3). It appeared around 250 nm and merged with another spectral peak around 720 nm.

The gold fill factor and depth that were used for these simulations was 0.55 and 130 nm, respectively. The gold fill factor value was chosen to be twice that of the silicon fill factor since historically we have seen that much undercut in deeply etched devices. The gold depth was chosen to be thick enough to not result in skin effects, but thin enough to not support an FP resonance on its own. Both these parameters

will perturb the phase of wave fronts pass through the top and bottom layers which will in turn shift where the FP resonance lies.

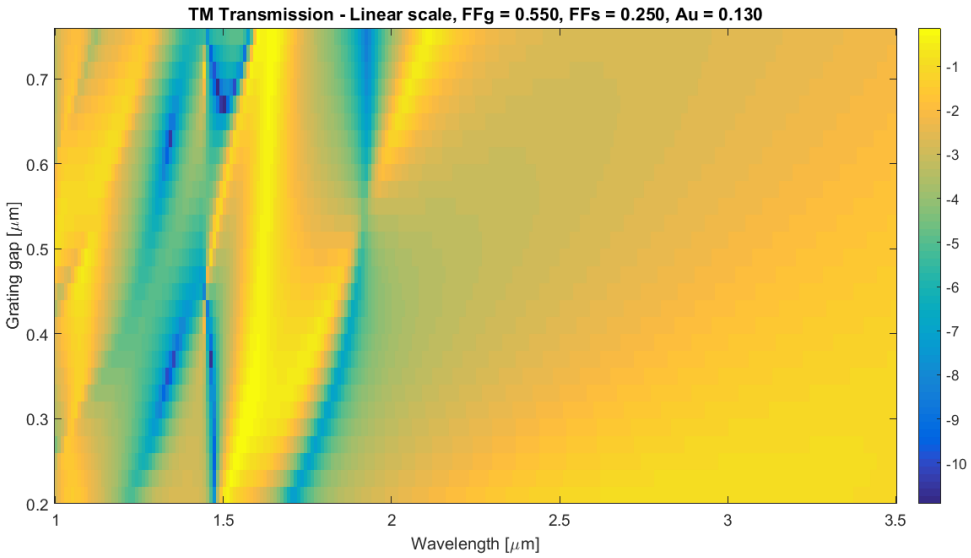


Figure 4.2: A log plot of the transmission spectra as a function of grating gap clearly shows transmission nulls at near 1.8 and 1.5 that correspond to SPP excitations. As the grating gap becomes smaller, the top SPP resonance begins to shift. This is expected since a smaller gap would result in model field coupling, changing the effective index of the middle material.

When we altered the the gold thickness we saw the peak shift in between the null points. If this effect were purely an FP resonance, its position in wavelength would be sensitive to both the gold depth and the grating gap (Figure 4.4). Figure 4.4 shows the effect of changing the gold height is shifting the position of the sharp spectral peak between the SPP minima. For gaps that are too small or too large, spurs that follow what appears to be FP peaks began to appear. These show up as wings on the side of the filter and are undesirable. Therefore, we want the gold depth that keeps the filter away from the anchor points and an etch depth such the filter shape is free from out-of-band wings (Figures 4.5 and 4.6).

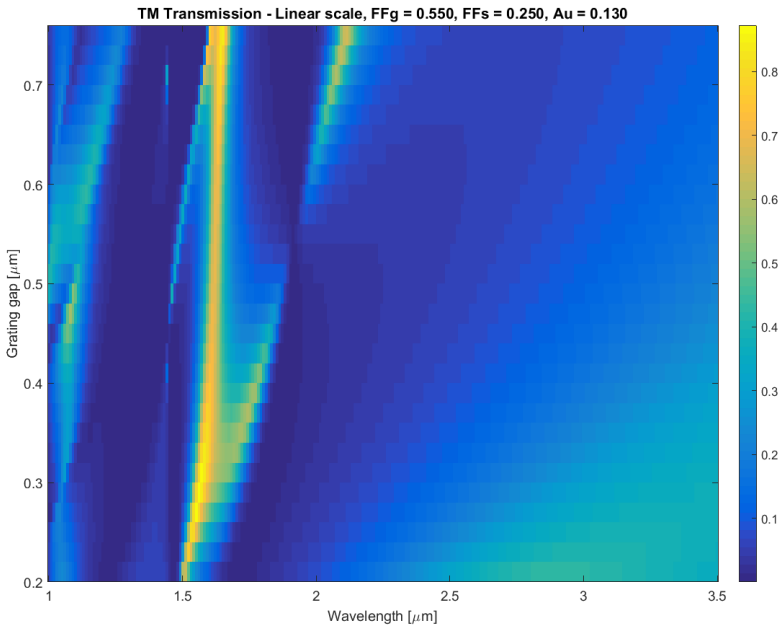


Figure 4.3: A linear plot of the transmission spectra show a sharp peak between the anchor points. The fact that the peak is independent of etch depth would allow us to use the etch as a parameter to improve the shape of the filter without shifting its position.

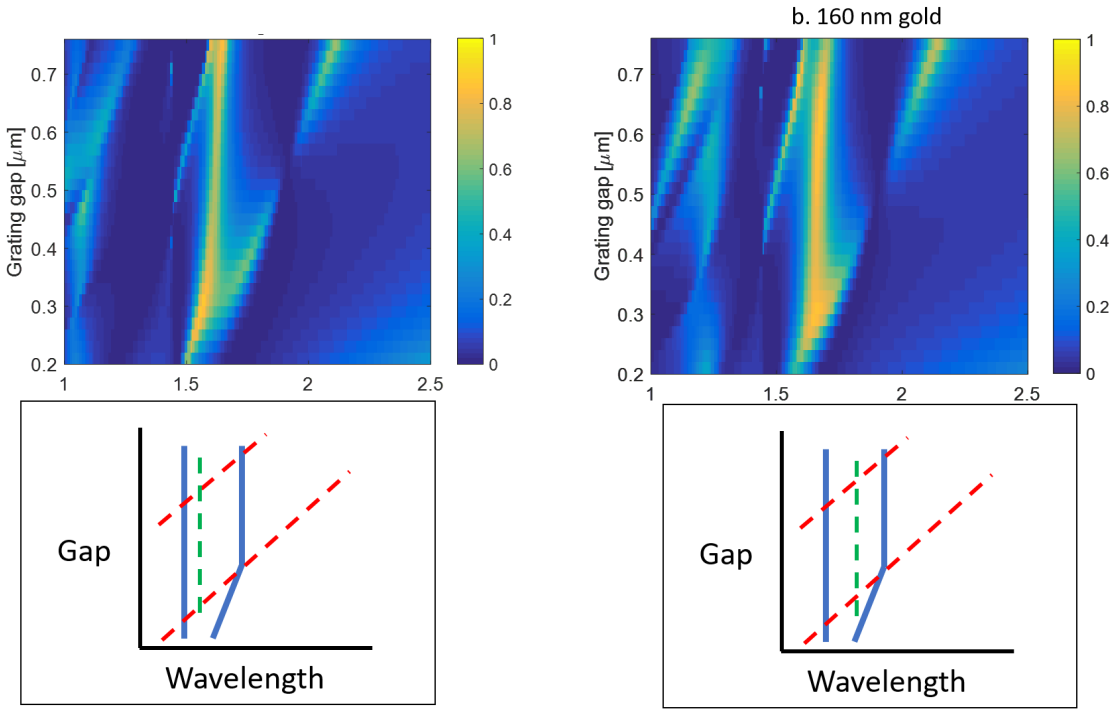


Figure 4.4: Holding everything else constant, changing the gold depth moves the location of the peak in between the two anchor points. This is useful both to keep the resonance away from the anchor points.

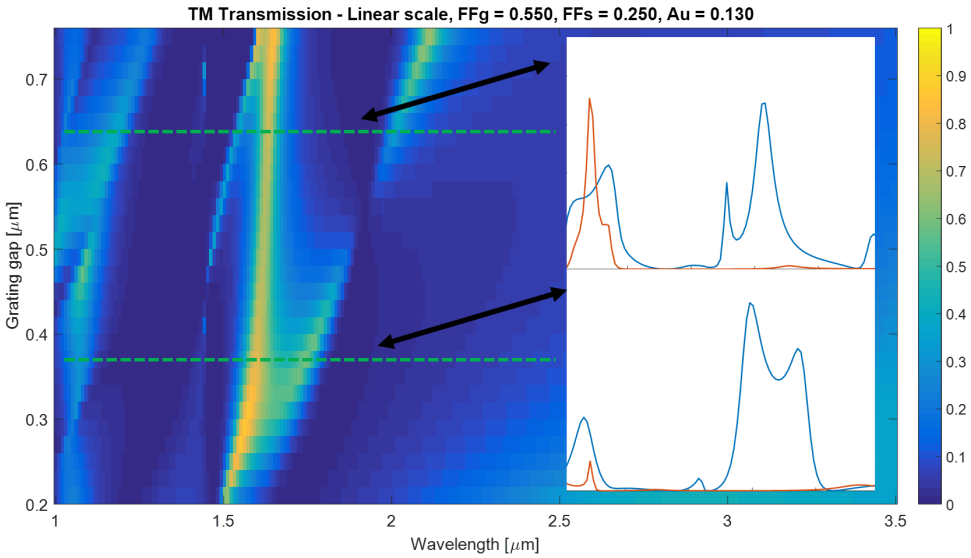


Figure 4.5: If the etch depth is too small or too large, wings appear either to the right or left of the main peak.

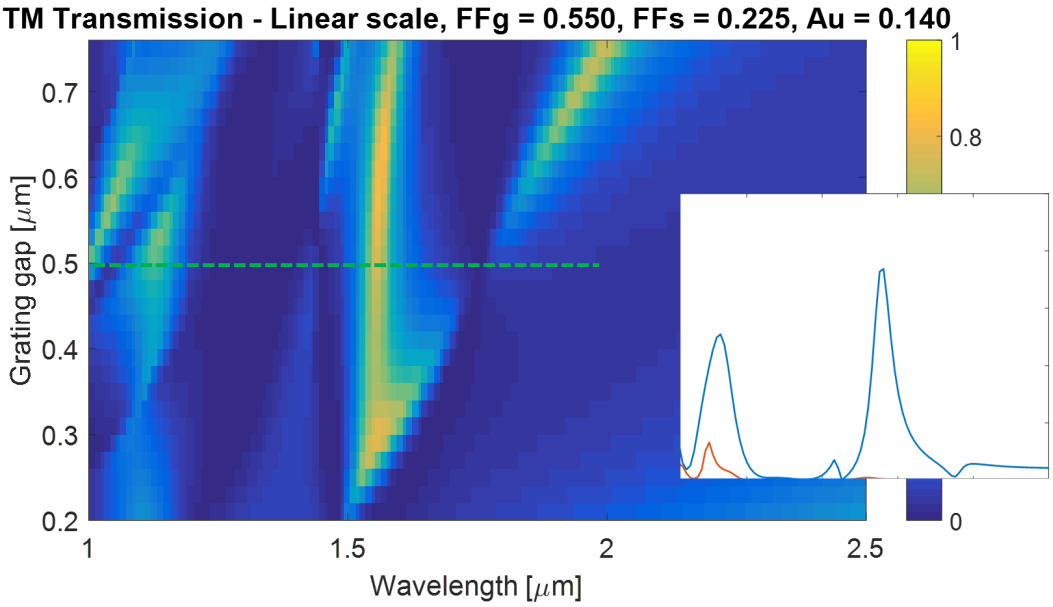


Figure 4.6: Choosing a middle etch depth far away from other FP resonances results in the best spectrum.

Global Optimization

All the effects of individual parameters got us remarkably close to a good filter design already. But in order to improve it further we had to do a global optimization of all parameters in parallel. This was needed because almost every parameter was coupled together. Altering the silicon fill factor changed the location of the rightmost SPP resonance but it will also shifted the FP resonance, as did the gold depth and gold fill factor. The effective index of the grating even had some period dependence since the zero-order approximation we started with was less valid for a grating that is greater than half the design wavelength.

Table 4.1: Global device optimization parameters

Parameter	Start	End	Number of points
Period	931 nm	980 nm	7
Si fill factor	20.7%	25.3%	7
Gap [nm]	423 nm	439 nm	7
Gold [nm]	120 nm	165 nm	10

Simulations were performed on these 2,340 devices with illumination ranging from 1 to 2 microns in 2-nm steps and at normal incidence. I first removed any devices that had a TM transmission of less than 60% and a FWHM of less than 120 nm. This reduced the number of passing devices to 2100.

Since it is difficult to quantify certain ideal filter properties, I went through the 2,100 remaining simulation results by hand scoring the spectra on a scale from 1 to 3. Figure 4.7 shows examples of good, decent, and bad filters. A score of 1 is given to a filter that has more than one undesirable property, like side lobes, or very low transmission. A score of 2 is a decent filter but might have a small out-of-band feature that may or may not be a problem. A score of 3 is a good filter, meaning it lacks the undesirable features described above. I then plotted these points in parameters

space. Since I have four parameters total, I held period constant and plotted other three parameters. But I found that the value of fill factor that produced good filters was 48%. If I deviated from this value in any direction the performance of the device would change drastically. Therefore it made more sense to plot period, gap, and metal thickness.

From Figures 4.8, 4.9, and 4.10 it is clear that the devices that perform the best form a linear region in parameter space. If we adjust the period, we must adjust the grating gap to compensate, and to a lesser degree, the gold depth. The absolute best devices in the region form this line in parameter space (4.11) and, when plotted, share almost identical properties save for a shift in wavelength (4.12).

Table 4.2: Optimized family of filters designs with peak TM transmission between 1527 nm and 1679 nm

Period [nm]	Etch [nm]	Gold [nm]	Peak TM wavelength [nm]
931	579	140	1527
947	594	140	1549
964	599	145	1581
980	615	145	1603
996	631	145	1625
1013	651	150	1651
1023	651	150	1679

Since we desired a device that would operate at 1.55 microns, we selected the second the devices in the family of curves of Figure 4.13. This device had a gold fill factor of 47%, silicon fill factor of 23.5%, etch depth of 595 nm, period of 947 nm and a gold depth of 140 nm. The ratio of peak TM transmission and TE transmission at the peak TM transmission gave an extinction ratio (ER) of 209.

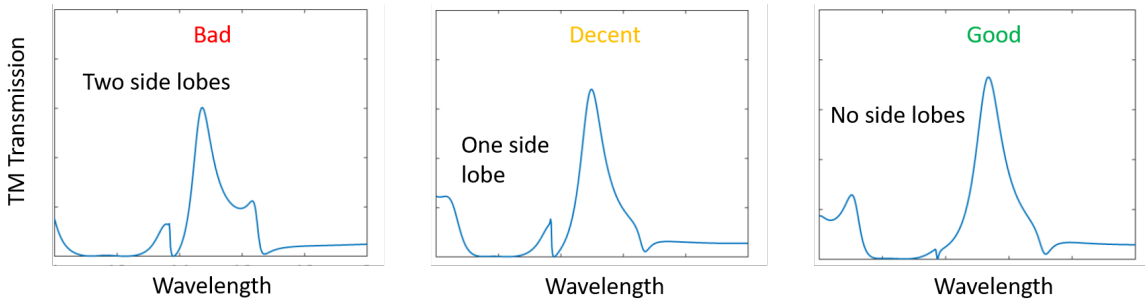


Figure 4.7: The results of the global optimization were scored by hand. A score of 1 was given to a bad filter that had multiple side lobes. A score of 2 was given to a filter that had only one small side lobe. A score of 3 was given to a filter with no side lobes.

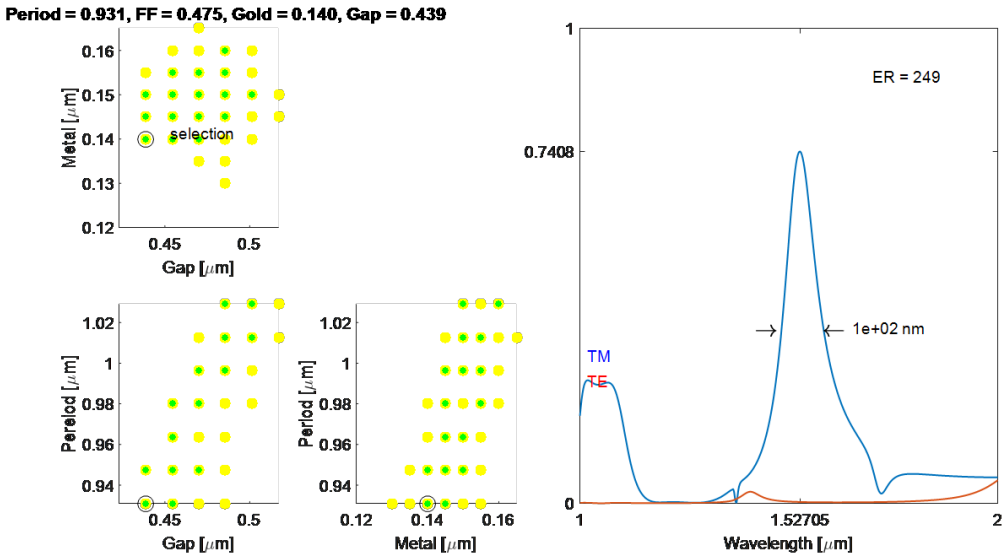


Figure 4.8: The left side of the figure is a three dimensional scatter plot of the located of decent (yellow) and good (green) devices. The right side of the figure shows the TM and TE spectra of the selected device along with its extinction ratio, spectral width, peak TM transmission, and wavelength of peak TM transmission.

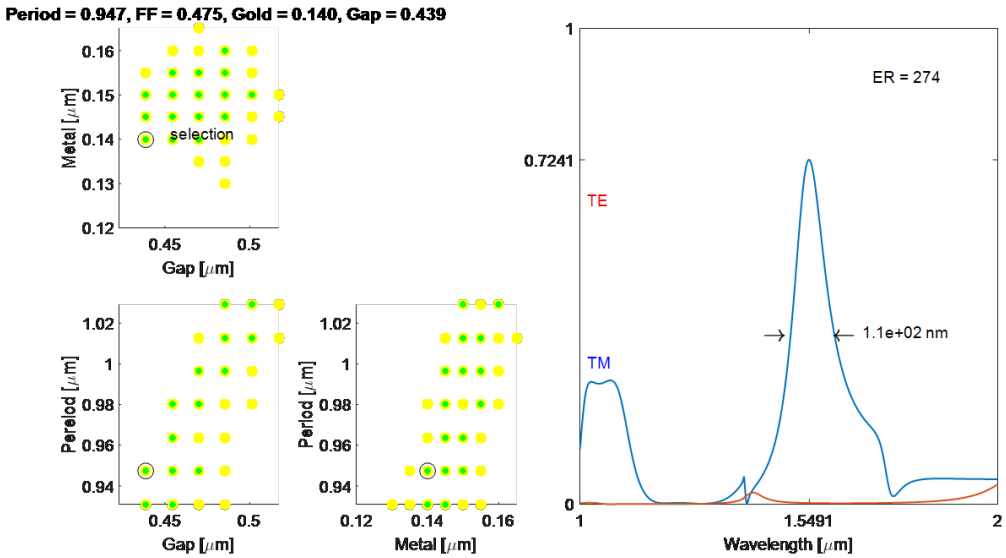


Figure 4.9: If I increase the period, but leave all the other parameters constant, the shape of the filter is slightly distorted.

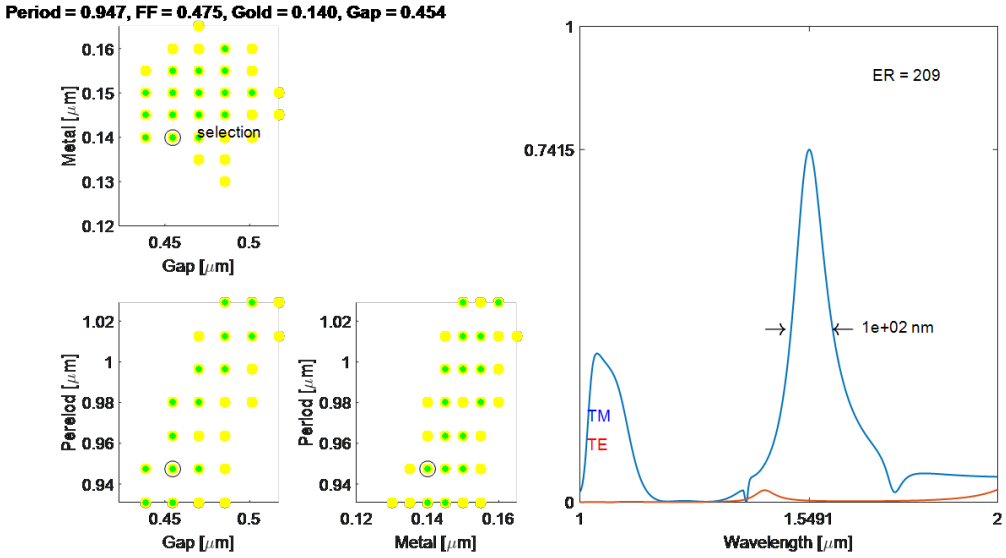


Figure 4.10: If I increase the grating gap after increasing the period, I recover the symmetric shape of the filter.

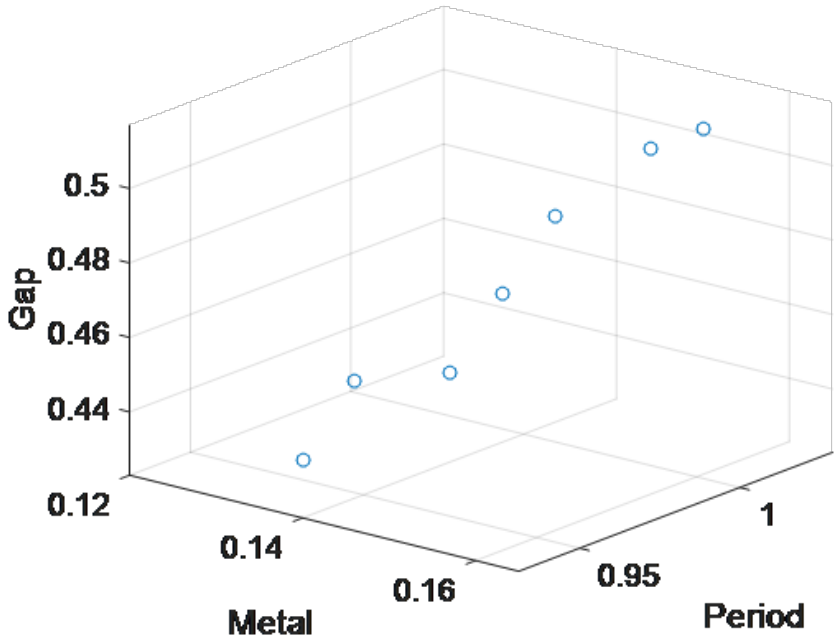


Figure 4.11: I've plotted the location of the most ideal filters, selecting them for symmetry. This shows the how devices with similar symmetry and peak transmission form a line in parameter space.

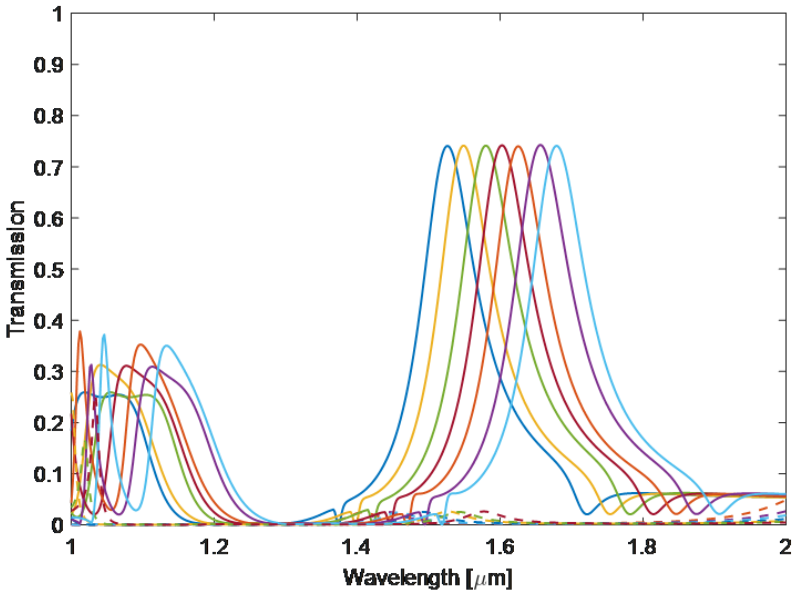


Figure 4.12: Plotting the spectra from the line of ideal devices, we see a family of curves that have almost identical filter properties but are shifted in wavelength.

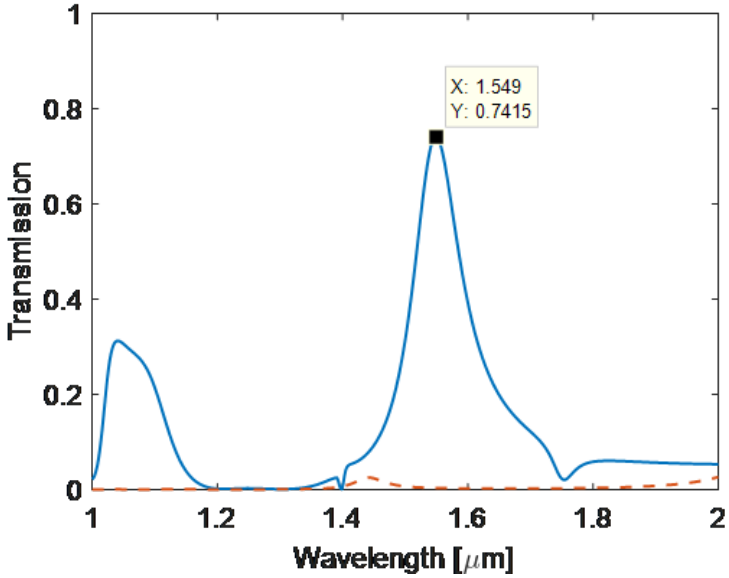


Figure 4.13: This device is optimized to operate at 1.55 microns. It has a fill factor of 47%, silicon fill factor of 23.5%, period of 947 nm, etch depth of 595 nm, and a gold depth of 140 nm.

Tolerance Analysis

The future performance of this device will depend on the how well each design parameter can be controlled in the fabrication process. Figure 4.14 shows that the tolerance in the gap between the gold gratings had minimal effect on device performance aside from the appearance of spurs on either side of the bandpass. Figure 4.15 shows a slightly larger effect caused by the uncertainty in the gold layer thickness. The presence of spurs reveals an effect similar to the gap tolerancing, but with the added effect of a shifting peak wavelength. Period had a large effect on the location of the peak TM transmission wavelength since it was the parameter that set the location of the anchor points (Figure 4.16). Fortunately, period is one of the most easily controlled and measured parameters. The fill factor of the gold (Figure 4.17) is less easily controlled than the period, but is easily measured.

The parameter that is most difficult to control is also one with the largest effect on device performance. The silicon fill factor - determined by how much undercut occurs during etching - is shown to greatly effect the location of the peak transmission as well as the shape of the bandpass (Figure 4.18).

Conclusion

By exploiting the narrowness of the silicon pillars, I was able to design a spectral bandpass filter, optimized for 1550-nm operation, that consists of silicon grating on a quartz substrate. Two of the four physical parameters were set first using theory. The remaining parameters were chosen based on RCWA simulations. Once the four parameters were chosen, the final device was found after a global optimization of all parameters found a family of identically performing devices.

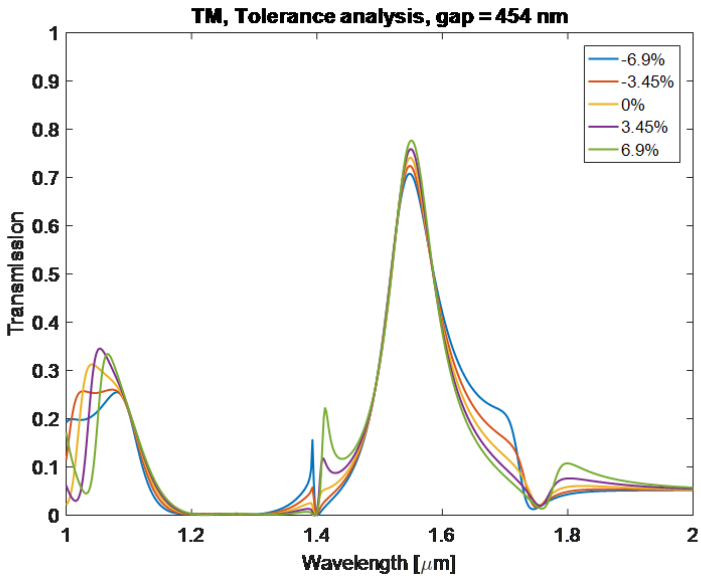


Figure 4.14: Uncertainty in the etching process would lead to uncertainty in the gap between the gratings. However, the nature of the resonance between the anchor points does not seem to be affected except for the appearance of spurs on either side of the bandpass.

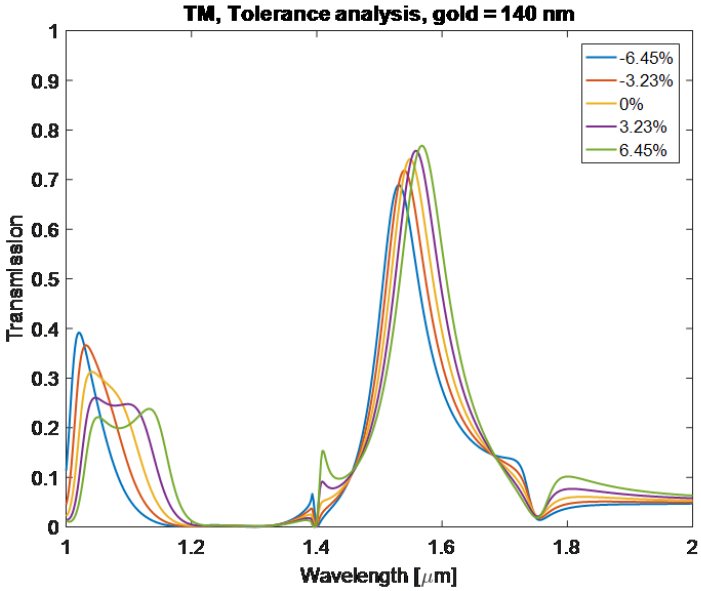


Figure 4.15: Uncertainty in the thickness of the gold leads both to peak shifting and the appearance of spurs on either side of the bandpass.

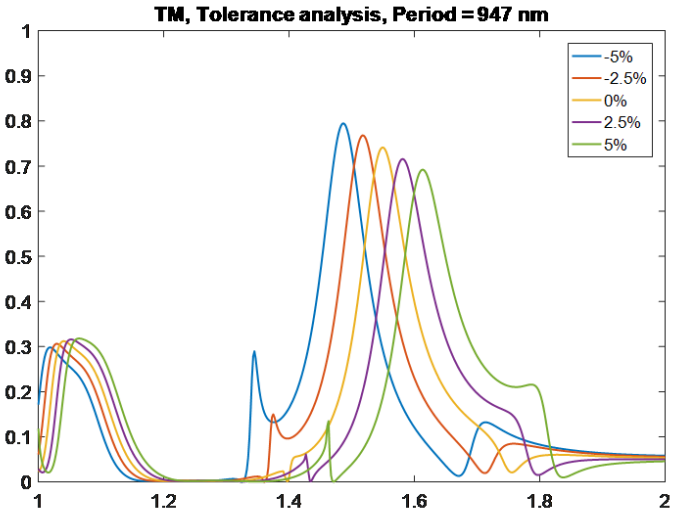


Figure 4.16: Period has quite a large effect on the location of the TM transmission peak since it determines the locations of the anchor points. However, period is an easily controlled and measured parameter.

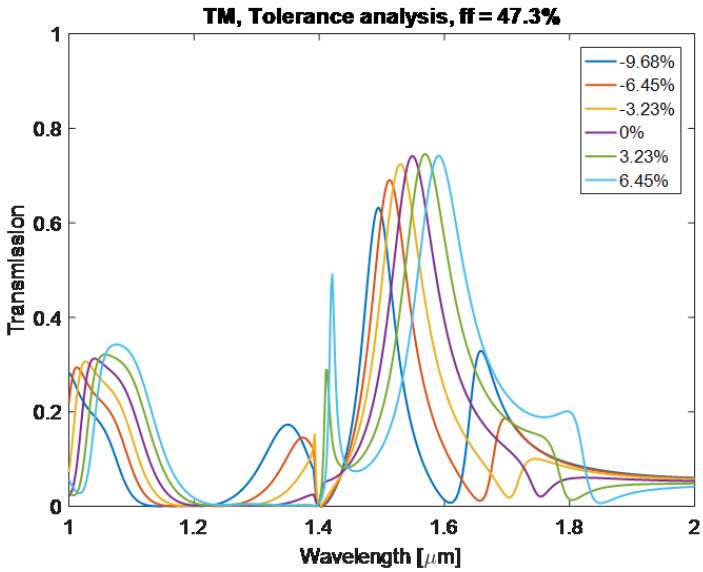


Figure 4.17: The gold fill factor effects the performance mainly because, if we assume a 2:1 undercut ratio, it will lead to an increase in the silicon pillar width. However, the gold fill factor, while less easily controlled than period, is easily measured.

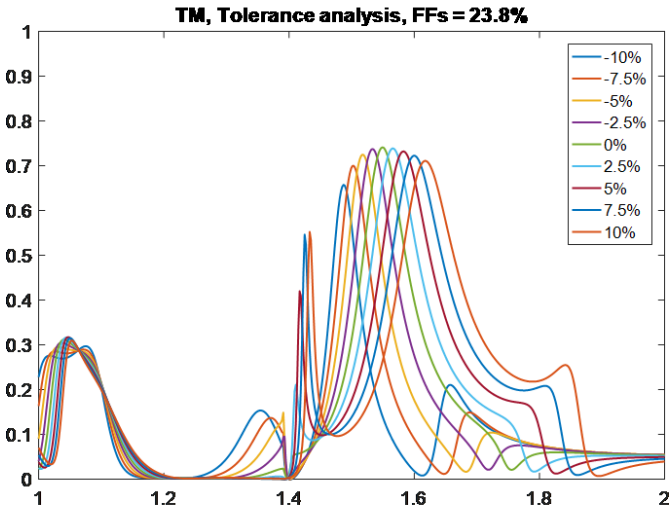


Figure 4.18: The silicon fill factor, equivalently the amount of undercut, has the largest effect both on the location of the peak TM transmission and the spectral bandpass shape.

Though this device resulted in a spectral bandpass of 100 nm, it is not an ideal design because any deviation from the ideal silicon fill factor would greatly alter the device performance. This involves precisely controlling the undercut of the device during etching, which would be difficult.

GENERAL DIELECTRIC DESIGN

Overview

Here I outline a deterministic design procedure that produces high TE rejection, narrow bandpass filter that has square grating walls provided we are able to create the dielectric grating between the gold gratings out of a material with an arbitrary refractive index.

Design Considerations

The silicon-on-glass design was capable of producing a bandpass filter of 100 nm. However, it suffered from one main drawback: the large dielectric constant of silicon required a small silicon fill factor in order to achieve the desired spectral selectivity. This wouldn't be a problem if the gold fill factor did not need to be large to achieve the desired TE rejection. The fact that we needed a large gold layer required the design to be undercut, which is difficult to control in fabrication. Moreover, the design achieved in the previous section was not easily tuned to a different wavelength as any change in the fill factor of the desired grating would very quickly destroy the resonance since the effective index of the cavity would be drastically altered.

Square Side Walls

Since it has been discussed that an undercut design has fabrication difficulties (albeit necessary for the silicon-on-quartz design) we will attempt to design for a device that has square side walls. We have the freedom to do this because we are free to choose the refractive index of our intermediate grating material. Recall how the undercut shape for the silicon-on-quartz design required an undercut because of the high index of silicon.

High Fill Factor

Recall that the largest contributer to high TE reflectivity is the rejection from the initial air/grating interface. The easiest way to ensure high TE rejection is by simply having a larger amount of that initial layer be metal. This is done by having a large fill factor. A higher fill factor has the added benefit of resulting in sharper TM peaks.

Variable Dielectric Constant for Grating

Since we have fixed, or at least restricted to a small range, the fill factor of the gratings, the parameter we will use to alter the relative position of the anchor points is the grating dielectric.

SPP Resonance Separation

Using zero-order effective medium theory, we can predict the position and more importantly the relative position of the SPP resonances. Working the other way, for a given SPP separation, we can compute the permittivity of the grating that would be required (We are assuming 1550-nm operation and that our substrate is still glass and therefore has a dielectric constant of around 1.5). Figure 5.1 shows how, for a given fill factor, smaller separations require a smaller permittivity. For a given separation, a larger fill factor requires a smaller permittivity.

Fill Factor Selection

Since the grating dielectric is a free parameter, fill factor is now decoupled from concerns of spectral selectivity. The walls of the device are square, so increasing the gold fill factor would also increase the silicon fill factor, but then the permittivity of the dielectric could be lowerd to compensate. Of course it is strictly true that the top

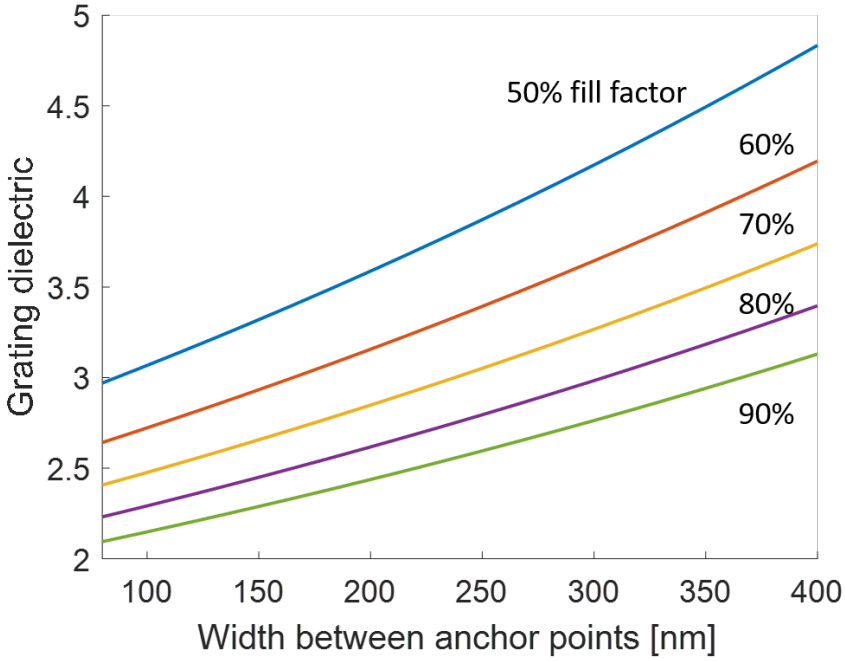


Figure 5.1: The required dielectric of the grating increases as a function of desired width between the SPP resonant wavelengths. For the same desired anchor point separation, a grating with a larger fill factor will require a lower dielectric.

and bottom gold layers will still perturb the phase of the TM modes, but in practice this effect is quite small. So now the fill factor is driven largely by TE rejection and should therefore be as large as possible.

Design Procedure

The design procedure started with a dielectric of variable index and depth deposited onto a glass substrate. Since we wanted filters at three wavelengths (1550 nm, 1640 nm, 1700 nm), we began with designing the 1700 nm filter. This was done so that we could ensure that no first-order diffraction occurred at wavelengths within the high pass filter; the designs at 1640 nm and 1550 nm will have smaller periods than the 1700-nm design. We also started with a 90% fill factor. This value is chosen so that we can ensure that any designs have the highest amount of TE rejection possible. The reason I didn't choose a value higher than 90% was to leave room for optimization. Since wavelength of peak response positively correlates to fill factor, the other two channels will have smaller fill factors. Were I to start the design procedure from lower fill factor, adjusting the fill factor to tune to a lower wavelength would destroy the polarization selectivity.

Figure 5.2 shows how the desired dielectric increases with SPP separation. This means for smaller SPP separations leading to narrower filters, we need a small as possible dielectric permittivity. However, smaller SPP separations require a larger period in order to keep them placed symmetrically around the design wavelength. Since we have a constraint that says we can't have first order diffraction above 1400 nm, we had a hard upper limit on the period we are able to use. From Figure 5.2, that limit is 942 nm, which corresponds to an anchor point separation of 600 nm and a grating dielectric permittivity of 4.68. Using values of gold thickness of 120 nm

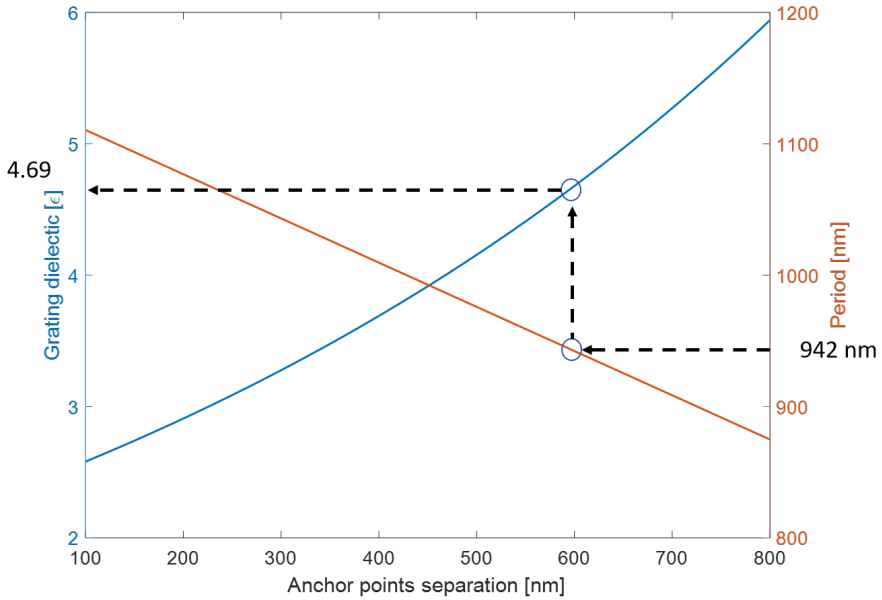


Figure 5.2: While the required grating dielectric will decrease as the anchor point separation decreases, the period must be increased in order to keep the anchor points symmetric about the design wavelength. Since we have a constraint of period at around 940 nm, this places a lower bound of 600-nm on the anchor point separation. 600-nm anchor point separation corresponds to a grating dielectric permittivity of 4.69.

that has achieved good results, we vary the grating gap until a symmetric resonance occurs between the two points (Figure 5.4)

From Figure 5.3 we see that the anchor points didn't appear at the exact location we predicted, but their separation is indeed 600 nm. To account for the offset, one could simply reduce the period, but it makes more sense to lower the permittivity of the grating which will blue shift the right anchor point until the midpoint of the two is located at 1700 nm. This new grating permittivity is found to be 3.68.

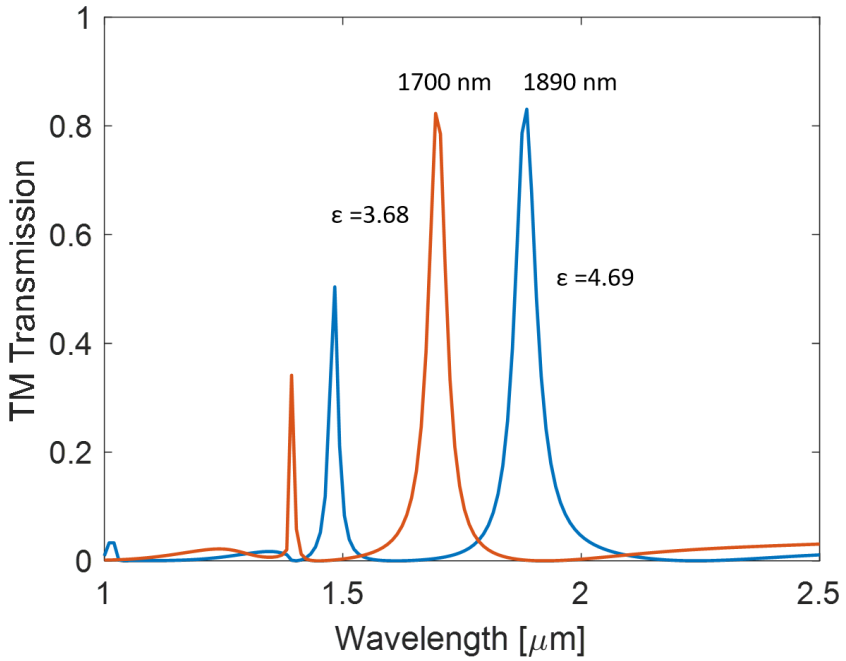


Figure 5.3: Separating the anchor points by 600 nm produced a very nice filter shape when the grating gap was at 650 nm and a gold thickness of 120 nm. The SPP anchor points were indeed separated by 600 nm, but their position, along with the FP peak, was off from theory by roughly 190 nm. Decreasing the grating dielectric from 4.69 to 3.68 was enough to bring the peak response to 1700 nm.

The gold thickness has two different main effects: 1) it changes that optimal grating gap value that produces the largest and narrowest passband, and 2) it changes the skewness of the that bandpass. Like in the previous chapter, the gold thickness

dictates where between the SPP resonances, the FP resonance occurs. The the most symmetric filters have the FP resonance occurring exactly in between the SPP resonances. Figure 5.5 shows that the optimum thickness is 100 nm of gold.

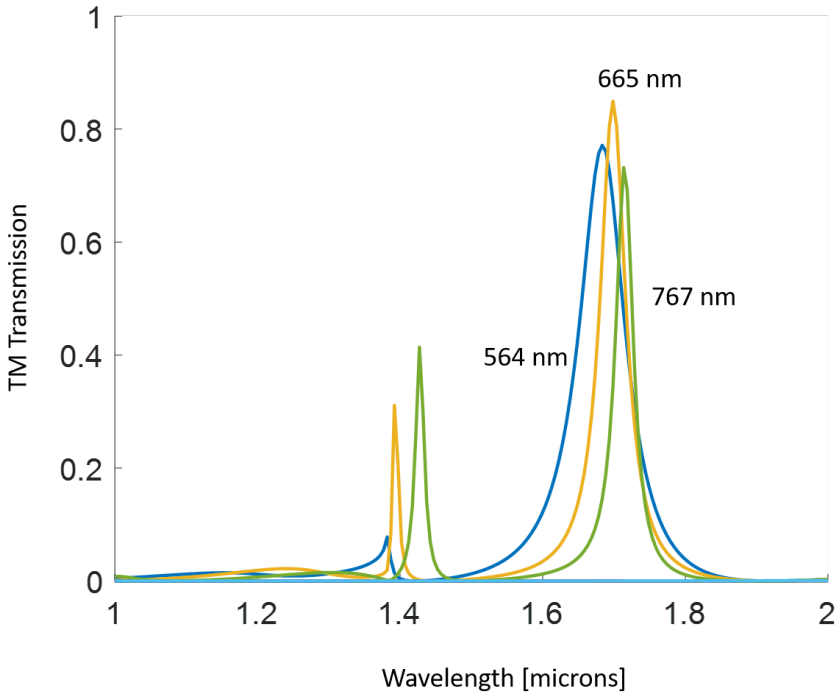


Figure 5.4: The proper grating gap separation is found by letting it vary until the most symmetric shape is found. Here I show the case for 100 nm of gold, a dielectric of 3.68. A grating gap of 564 nm creates a broader spectral response. The most symmetric shape is found at a gap of 665 nm. If we increase much further, the response begins to roll off (767 nm).

From this 1700-nm design, the period can be adjusted to change the peak response wavelength. This reduces the transmission peak slightly, so fill factor is used to correct this. This is an iterative process since fill factor also slightly shifts the wavelength of peak response.

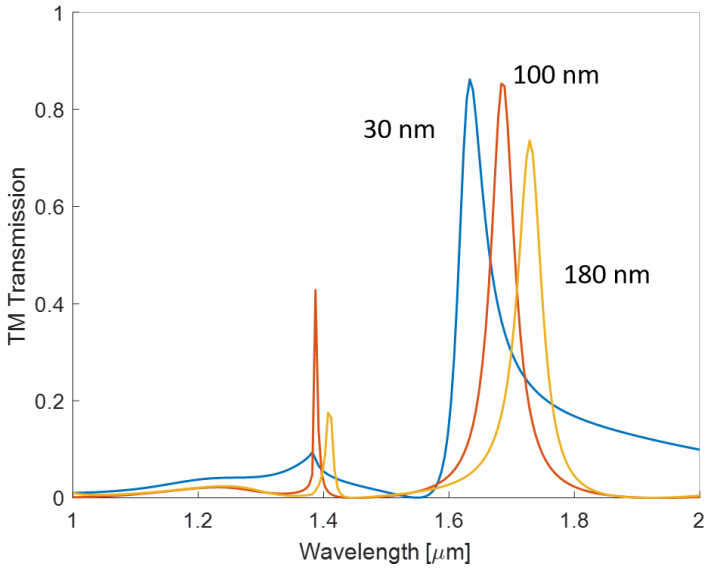


Figure 5.5: Gold depth effects the symmetry of the FP peak between the anchor points. For each depth of gold, the gap was varied to produce the most symmetric spectral peak. For 30 nm of gold, the "best" shape is highly asymmetric, with the top spectral peak closer to the left anchor point. For 180 nm of gold, the peak is asymmetric but now closer to the right anchor point. 100 nm of gold was found to produce the most symmetric shape.

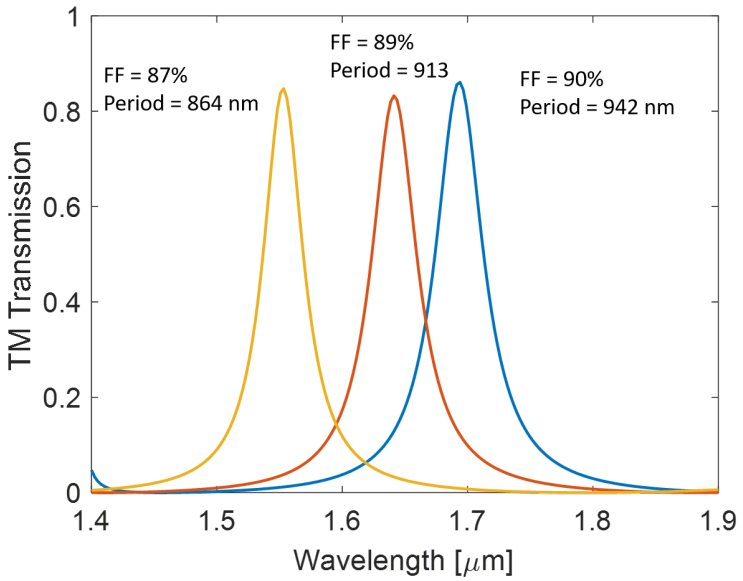


Figure 5.6: Since I planned on the maximum fill factor and period to be at the 1700 nm wavelength, we are left with plenty of room to change both parameters to arrive at filters for the other two wavelengths, 1640 nm and 1550 nm. All the filters nave a peak transmission of roughly 85% with a FWHM of between 40 and 50 nm.

Parameter Optimization

Each channel was optimized individually around the design parameters from Figure 5.6. Period was held constant since it was most weakly coupled to bandpass shape and since we have strict requirements on first order diffraction that restrict us to a maximum period. It was used at the end to tweak the wavelength of peak response if necessary.

The parameters used in the optimization can be seen in Tables 5.1, 5.2, and 5.3. The only difference between each channel is the period value used and the range of fill factors.

The results of the simulation were sifted by selecting only results that met certain criteria. The first three criteria in Table 5.4 ensured all results had high and narrow bandpass shapes around the corresponding design wavelength. The final criterion

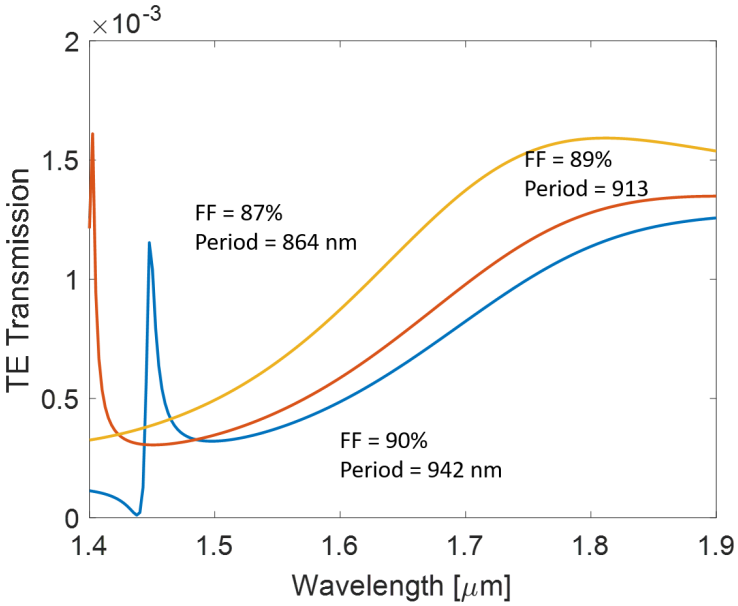


Figure 5.7: Since we are using such high fill factors, the TE response is very low, with peak extinction ratios of between 550 for the 1550-nm channel, to almost 1500 for the 1700-nm channel. Nowhere in the band of interest does the TE transmission rise about 0.2%

Table 5.1: 1700-nm parameter optimization

Parameter	Start	End	Number of points
ϵ	3.54	3.92	7
Fill factor	85.5%	94.5%	7
Gap [nm]	632	698	7
Gold [nm]	90	110	7
Period [nm]	942	942	1

Table 5.2: 1640-nm parameter optimization

Parameter	Start	End	Number of points
ϵ	3.54	3.92	7
Fill factor	84.5%	93.5%	7
Gap [nm]	632	698	7
Gold [nm]	90	110	7
Period [nm]	913	913	1

Table 5.3: 1550-nm parameter optimization

Parameter	Start	End	Number of points
ϵ	3.54	3.92	7
Fill factor	82.7%	91.4%	7
Gap [nm]	632	698	7
Gold [nm]	90	110	7
Period [nm]	864	864	1

was based on the fact that we have to fabricate these three channels on the same substrate. The reason that gold is not included at this stage is because it is weakly coupled to performance.

Table 5.4: Selection criteria

Parameter	Criterion
Peak TM transmission	greater than 75%
FWHM	less than 40 nm
Wavelength of peak transmission	+/- 1 nm of design
Gap distance and grating ϵ	Must be common between three wavelengths

The results (Table 5.5) of this selection process show that a gap of 687 nm and a grating dielectric of 3.69 are optimal. The optimal gold values were different for each channel (93 nm, 97 nm, 107 nm).

Table 5.5: Optimization results

Channel	Period [nm]	FF [%]	Gap [nm]	ϵ	Gold [nm]
1550	864	88.5	687	3.69	93
1640	913	90.5	687	3.69	97
1700	942	91.5	687	3.69	107

Since the gold depth must be common between all three channels, I chose use the average gold depth (99 nm) and adjust the period by 1-4 nm to account for the slight wavelength shift that occurred at the 1550-nm and 1700-nm channel. A negligible

shift occurred at the middle wavelength because the gold depth had changed by only 2 nm.

Figure 5.8 shows the spectra before and after this parameter optimization process. The major improvement is the FWHM on each channel was reduced by 8-10 nm while suffering only a slight decrease in absolute transmission. Table 5.6 shows the design parameters and spectral width of each channel.

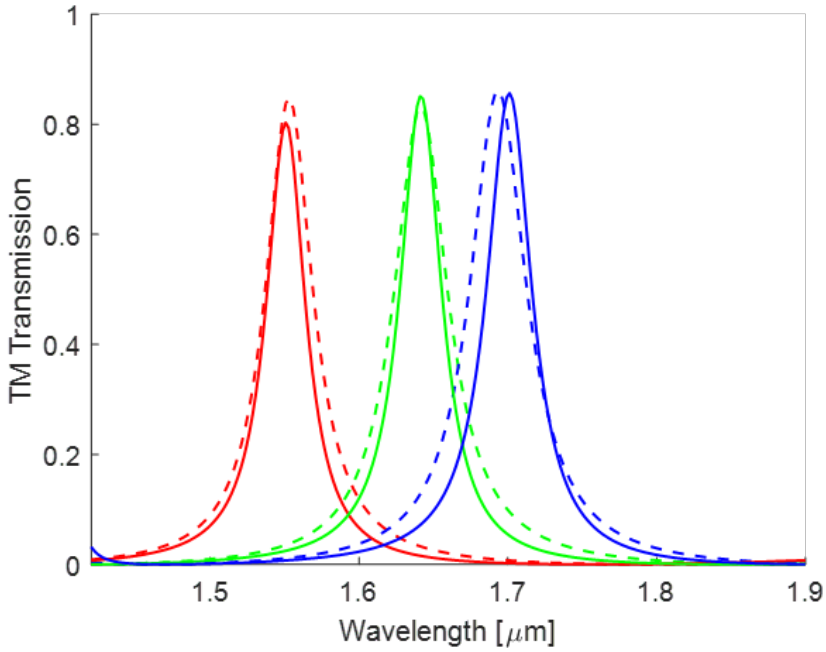


Figure 5.8: Spectral shapes of the three channels before (dashed) and after (solid) optimization: 1550 nm in red, 1640 nm in gree, 1700 nm in blue. The optimization led to a decrease in bandpass width. 1550-nm design has a peak transmission of 80% and a FWHM of 32 nm. 1640-nm design has a peak transmission of 85% and a FWHM of 36 nm. 1700-nm design has a peak transmission of 86% and a FWHM of 38 nm.

Table 5.6: Final optimization results

Channel	Period [nm]	FF [%]	Gap [nm]	ϵ	Gold [nm]	FWHM [nm]	ER
1550	863	88.5	687	3.69	99	32	1687
1640	913	90.5	687	3.69	99	36	1567
1700	946	91.5	687	3.69	99	38	1393

Conclusion

What was achieved are three devices with peak transmission greater than 80% with a FWHM of less 40 nm. The extinction ratio at the peak TM transmission wavelength were all well above 1000. Three devices were designed such that they could be fabricated on a single chip. Each device shared the same etch depth, gold depth, and grating dielectric, requiring only a different period and fill factor to tune between channels. High TE rejection (TE transmission less than 0.2%) was achieved by having the fill factors as close to 90% as possible.

In addition to great spectral performance, the devices had the added benefit of being easier to fabricate than the silicon-on-quartz device that was designed in the previous chapter. Recall that the undercut in the silicon-on-quartz device was necessary in order to reduce the effective index of the cavity. Since we are free to choose the grating dielectric, we are free to force the device to have square walls, which is easier to control in fabrication. The devices would require a 786-nm layer of dielectric deposited on a quartz substrate. The cross sections of the final devices can be seen in Figures 5.9, 5.10, and 5.11. Although the final fill factors were high, they would result in an 8:1 etch ratio which is achievable.

The grating dielectric of 3.69 (n = 1.92) that we arrived at is achievable since we know that non-stoichiometric silicon nitride (normally n = 2) films are possible using Si doping after chemical vapor deposition [43].

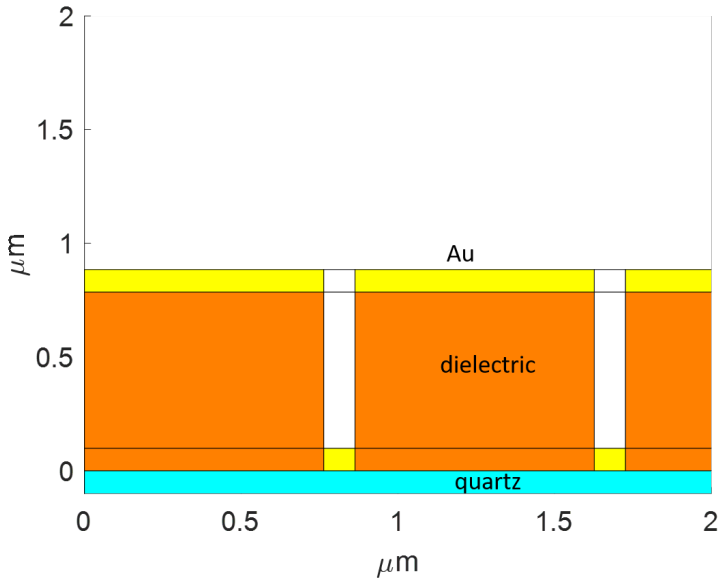


Figure 5.9: A cross section of the 1550-nm design.

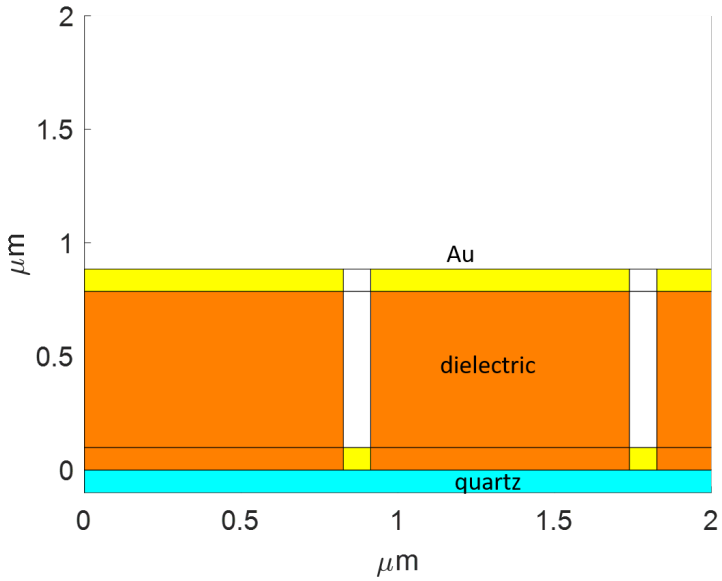


Figure 5.10: A cross section of the 1640-nm design.

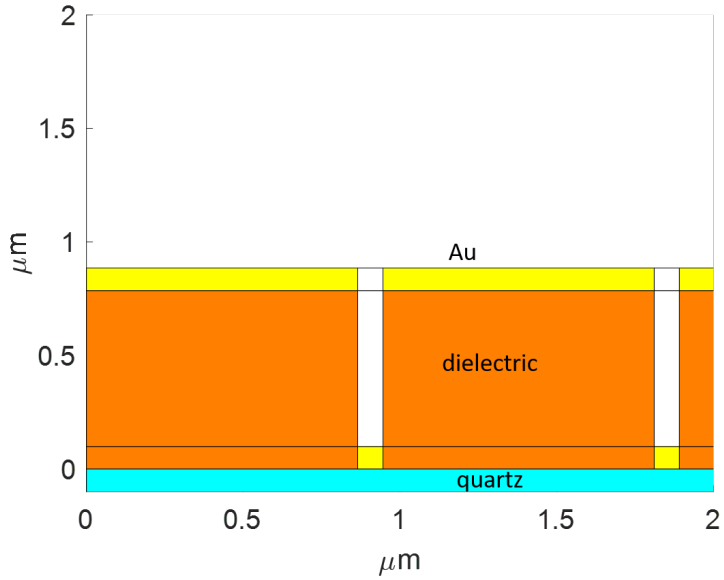


Figure 5.11: A cross section of the 1700-nm design.

CONCLUSION

Summary

The project called for a family of optical filters that are capable of measuring the first three Stokes' parameters (S_0, S_1, S_2) of incident light at three wavelengths, 1550 nm, 1640 nm, and 1700 nm using wavefront division multiplexing. I have demonstrated that this is possible using two-layer, two-material metallic gratings.

I outlined the theory of how these devices function as both polarizers and spectral bandpass filters. By strategically placing the SPP resonances on either side of the FP, we can reduce the out-of-band transmission and narrow the passband.

For the single material polarizing bandpass filters I demonstrate that we have good agreement between experiment and simulation once we account for the non-square shape of the silicon grating rulings and the highly uncertain gold material properties.

I show how a silicon-on-quartz polarizing bandpass filter is possible if we intentionally introduce an undercut design to reduce the effective index of the cavity. Through global optimization of all parameters I was able to arrive a device optimized for operation at 1550 nm with a FWHM of 100 nm.

By choosing a dielectric material for the grating that is closer to that of silicon nitride, I was able to design, in a mostly deterministic fashion, three devices optimized for operation at 1550 nm, 1640 nm, and 1700 nm that are able to be fabricated on the same chip. All three passband shapes had a peak TM transmission of higher than 80% and TE transmission of less than 0.2%. All three had a FWHM of less than 40 nm.

The fact that the optimization process in the previous chapter resulted in an only slight improvement in device performance is evidence of the robustness of the

design procedure. With slight modification, this procedure could be used to design filters at arbitrary wavelengths, though the dispersion of the materials must be taken into account.

Discussion

This work has presented a family of devices that can be used in recovering the first three Stokes' parameters of incident light at three different wavelengths which would be crucial in remotely and passively determining the phase of cloud water. These devices share design parameters that make them ideal for fabrication on a common substrate, meaning they can be easily made into an array for mating with a matched array of detectors. This array of detectors would have to be paired with a longpass optical filter that would block out any wavelengths shorter than 1400 nm. This is done to ensure that light of a short enough wavelength does not diffract off the devices or introduce additional noise into the spectral-polarimetric measurement. The gratings begin to transmit again at wavelengths longer than 1900 nm, but typical InGaAs photodetectors cutoff around that region.

In arriving at these designs I have illustrated the effect that each grating parameter has on the transmission spectra, both in TE and TM. Since each parameter often affects more than one characteristic (peak transmission, spectral bandpass, TE rejection), it was further necessary to develop a design process that nearly decoupled them.

One major contribution I made to this NASA project include identifying the importance of SPPs and how they can be used to improve the spectral bandpass shape by suppressing the TM transmissions at desired wavelengths. This would ultimately lead to the two-material design. Another contribution was identifying the cause of

the discrepancy between simulation and experiment. This would lead to having a deeper understanding of the role each parameter played in device performance.

Future Work

The final three device designs were done without considering dispersion. This was done intentionally to highlight the physics of device operation. Moreover, the materials were chosen to be minimally dispersive over the range of 1400 nm to 1900 nm. I am confident that a global parameter optimization of the device parameters that includes dispersion starting from my dispersion-less design will yield good results without much of a change in performance.

Currently, the fabrication process for fabricating the two-material devices is underway at Montana State University. Changing from the silicon substrate to quartz substrate introduced difficulties in lithography since the substrate is no longer conductive. We are also still investigating ways of coating quartz substrates with doped silicon nitride.

Once we have fabricated and optically characterized multiple single arrays at various orientations, the next step would be to send the design to a different facility for large scale array fabrication. There also remain higher system design considerations to account for (configuration of superpixels, method of mounting to detectors, optics) before this system will be ready for field testing.

The specific wavelengths used in this design process were chosen specifically for the cloud phase application. In principle, any wavelength or range of wavelengths could be used. This design could easily be modified to function in the visible spectrum. Instead of making spectral bandpass shapes as narrow as possible, they could intentionally be made to cover a entire color ranges (red, green, blue). These could be used for visual polarimetry or for LCD technology.

It is also worth exploring the possibility of adding another layer to the device in order to discern right-hand or left-hand circular polarized light.

REFERENCES CITED

[1] Donald Wylie, Darren L. Jackson, W. Paul Menzel, and John J. Bates. Trends in global cloud cover in two decades of HIRS observations. *Journal of Climate*, 18(15):3021–3031, 2005.

[2] Michael D. King. Radiative Properties of Clouds. In Peter V. Hobbs, editor, *Aerosol-Cloud-Climate Interactions*, pages 123–149. Academic Press, 1993.

[3] Kenneth Sassen. The polarization lidar technique for cloud research: A review and current assessment. *Bulletin of the American Meteorological Society*, 72(12):1848–1866, 1991.

[4] K. Knobelspiesse, B. van Diedenhoven, A. Marshak, S. Dunagan, B. Holben, and I. Slutsker. Cloud thermodynamic phase detection with polarimetrically sensitive passive sky radiometers. *Atmospheric Measurement Techniques*, 8(3):1537–1554, 2015.

[5] Bahaa E.A Saleh and Malvin Carl Teich. *Fundamentals of Photonics*. John Wiley & Sons, Hoboken, second edition, 2007.

[6] David Riesland. Infrared Cloud Imaging Systems Characterization. Master's thesis, Montana State University, 2016.

[7] Dennis H. Goldstein. Stokes Polarimetry. In *Polarized Light*, pages 327–351. CRC Press, Boca Raton, third edition, 2011.

[8] J. Scott Tyo, Dennis L. Goldstein, David B. Chenault, and Joseph A. Shaw. Review of passive imaging polarimetry for remote sensing applications. *Appl. Opt.*, 45(22):5453–5469, Aug 2006.

[9] 4D Technology. PolarCam.

[10] Jing Zhou and L. Jay Guo. Transition from a spectrum filter to a polarizer in a metallic nano-slit array. 4:3614 EP –, Jan 2014. Article.

[11] Zhenyue Luo, Guiju Zhang, Ruidong Zhu, Yating Gao, and Shin-Tson Wu. Polarizing grating color filters with large acceptance angle and high transmittance. *Appl. Opt.*, 55(1):70–76, Jan 2016.

[12] Jinkui Chu, Yingjie Zhang, Zhiwen Wang, and Le Guan. Polarizing color filter based on subwavlength metallic grating with grooves carved in. *Optics Communications*, 315:32–36, 2014.

[13] Nghia Nguyen-Huu, Yu-Lung Lo, Yu-Bin Chen, and Tsai-Yu Yang. Realization of integrated polarizer and color filters based on subwavelength metallic gratings using a hybrid numerical scheme. *Appl. Opt.*, 50(4):415–426, Feb 2011.

[14] Nanling Sun, Jie Cui, Yi She, Lan Lu, Jun Zheng, and Zhicheng Ye. Tunable spectral filters based on metallic nanowire gratings. *Optical Materials Express*, 5(4):912, 2015.

[15] Stephan Junger, Wladimir Tschekalinksij, Nanko Verwaal, and Norbert Weber. Polarization and spectral filter arrays based on sub-wavelength structures in CMOS. In *OPTO*, pages 1–5, Nurnberg, 2011.

[16] Sergey Gorelick, Vitaliy A Guzenko, Joan Vila-Comamala, and Christian David. Direct e-beam writing of dense and high aspect ratio nanostructures in thick layers of pmma for electroplating. *Nanotechnology*, 21(29):295303, 2010.

[17] Max Born and Emil Wolf. *Principles of Optics*. Cambridge University Press, Cambridge, seventh edition, 1959.

[18] Ivan Richter, Pang-Chen Sun, Fang Xu, and Yeshayahu Fainman. Design considerations of form birefringent microstructures. *Appl. Opt.*, 34(14):2421–2429, May 1995.

[19] Philippe Lalanne and Jean-Paul Hugonin. High-order effective-medium theory of subwavelength gratings in classical mounting: application to volume holograms. *J. Opt. Soc. Am. A*, 15(7):1843–1851, Jul 1998.

[20] George R. Bird and Maxfield Parrish. The wire grid as a near-infrared polarizer. *J. Opt. Soc. Am.*, 50(9):886–891, Sep 1960.

[21] Eugene Hecht. *Optics*. Addison-Wesley, third edition, 1998.

[22] Heinz Raether. *Surface Plasmons on Smooth and Rough Surfaces and on Gratings*. Springer Berlin Heidelberg, 1988.

[23] Sergey Gaponenko. *Introduction to Nanophotonics*. Cambridge University Press, first edition, 2010.

[24] Bo Liedberg, Claes Nylander, and Ingemar Lunstrm. Surface plasmon resonance for gas detection and biosensing. *Sensors and Actuators*, 4:299 – 304, 1983.

[25] E. Hutter and J.H. Fendler. Exploitation of localized surface plasmon resonance. *Advanced Materials*, 16(19):1685–1706, 2004.

[26] M. G. Moharam and T. K. Gaylord. Diffraction analysis of dielectric surface-relief gratings. *J. Opt. Soc. Am.*, 72(10):1385–1392, Oct 1982.

[27] M. G. Moharam, T. K. Gaylord, Eric B. Grann, and Drew A. Pommet. Formulation for stable and efficient implementation of the rigorous coupled-wave analysis of binary gratings. *J. Opt. Soc. Am. A*, 12(5):1068–1076, May 1995.

[28] Nicolas Chateau and Jean-Paul Hugonin. Algorithm for the rigorous coupled-wave analysis of grating diffraction. *J. Opt. Soc. Am. A*, 11(4):1321–1331, Apr 1994.

[29] Lifeng Li. Use of fourier series in the analysis of discontinuous periodic structures. *J. Opt. Soc. Am. A*, 13(9):1870–1876, Sep 1996.

[30] Vincent Paeder. *Bloch Surface Wave Biosensing: Study of Optical Elements for the Early Detection of Protein Aggregation*. PhD thesis, École polytechnique fédérale de Lausanne, 2011.

[31] Jerry Sheehan and Pol Llovet. Hyalite High-Performance Computing System.

[32] Eugene Hecht. *Optics*. Addison-Wesley, third edition, 1998.

[33] Qing Cao and Philippe Lalanne. Negative role of surface plasmons in the transmission of metallic gratings with very narrow slits. *Physical review letters*, 88(5):057403, 2002.

[34] Robert L. Olmon, Brian Slovick, Timothy W. Johnson, David Shelton, Sang-Hyun Oh, Glenn D. Boreman, and Markus B. Raschke. Optical dielectric function of gold. *Phys. Rev. B*, 86:235147, Dec 2012.

[35] A D Rakic, A B Djurisic, J M Elazar, and M L Majewski. Optical properties of metallic films for vertical-cavity optoelectronic devices. *Applied optics*, 37(22):5271–5283, 1998.

[36] Kevin M. McPeak, Sriharsha V. Jayanti, Stephan J P Kress, Stefan Meyer, Stelio Iotti, Aurelio Rossinelli, and David J. Norris. Plasmonic films can easily be better: Rules and recipes. *ACS Photonics*, 2(3):326–333, 2015.

[37] Shaista Babar and J. H. Weaver. Optical constants of cu, ag, and au revisited. *Appl. Opt.*, 54(3):477–481, Jan 2015.

[38] Wolfgang S. M. Werner, Kathrin Glantschnig, and Claudia Ambrosch-Draxl. Optical constants and inelastic electron-scattering data for 17 elemental metals. *Journal of Physical and Chemical Reference Data*, 38(4):1013–1092, 2009.

[39] Martin A. Green and Mark J. Keevers. Optical properties of intrinsic silicon at 300 k. *Progress in Photovoltaics: Research and Applications*, 3(3):189–192, 1995.

[40] H. H. Li. Refractive index of silicon and germanium and its wavelength and temperature derivatives. *Journal of Physical and Chemical Reference Data*, 9(3):561–658, 1980.

[41] D. T. Pierce and W. E. Spicer. Electronic structure of amorphous si from photoemission and optical studies. *Phys. Rev. B*, 5:3017–3029, Apr 1972.

[42] Calvin D. Salzberg and John J. Villa. Infrared refractive indexes of silicon germanium and modified selenium glass*. *J. Opt. Soc. Am.*, 47(3):244–246, Mar 1957.

[43] O. Blazquez, J. Lopez-Vidrier, S. Hernandez, J. Montserrat, and B. Garrido. Electro-optical properties of non-stoichiometric silicon nitride films for photovoltaic applications. *Energy Procedia*, 44:145 – 150, 2014. Proceedings of E-MRS Spring Meeting 2013 Symposium D Advanced Inorganic Materials and Structures for Photovoltaics 27-31 May 2013, Strasbourg, France.